

Warm early Mars surface enabled by high-altitude water ice clouds

Edwin S. Kite^{a,1} , Liam J. Steele^{a,2} , Michael A. Mischna^b , and Mark I. Richardson^c 

^aDepartment of the Geophysical Sciences, University of Chicago, Chicago, IL 60615; ^bJet Propulsion Laboratory, California Institute of Technology, Pasadena, CA 91109; and ^cAeolis Research, Chandler, AZ 85224

Edited by Mark Thiemens, University of California San Diego, La Jolla, CA, and approved March 10, 2021 (received for review February 4, 2021)

Despite receiving just 30% of the Earth's present-day insolation, Mars had water lakes and rivers early in the planet's history, due to an unknown warming mechanism. A possible explanation for the >10²-y-long lake-forming climates is warming by water ice clouds. However, this suggested cloud greenhouse explanation has proved difficult to replicate and has been argued to require unrealistically optically thick clouds at high altitudes. Here, we use a global climate model (GCM) to show that a cloud greenhouse can warm a Mars-like planet to global average annual-mean temperature (\bar{T}) ~265 K, which is warm enough for low-latitude lakes, and stay warm for centuries or longer, but only if the planet has spatially patchy surface water sources. Warm, stable climates involve surface ice (and low clouds) only at locations much colder than the average surface temperature. At locations horizontally distant from these surface cold traps, clouds are found only at high altitudes, which maximizes warming. Radiatively significant clouds persist because ice particles sublimate as they fall, moistening the subcloud layer so that modest updrafts can sustain relatively large amounts of cloud. The resulting climates are arid (area-averaged surface relative humidity ~25%). In a warm, arid climate, lakes could be fed by groundwater upwelling, or by melting of ice following a cold-to-warm transition. Our results are consistent with the warm and arid climate favored by interpretation of geologic data, and support the cloud greenhouse hypothesis.

Mars | planetary habitability | paleoclimate

Mars is cold today, but early Mars was warm enough for lakes (e.g., ref. 1) that were habitable (2). These early (4 to <3 Ga) warm climates cannot be explained by basic models of the early Mars greenhouse effect (involving only CO₂ and H₂O vapor) because these predict climates that are too cold (3, 4). Hypotheses for solving this problem have difficulty in explaining the geologic evidence for >10²-y-long lake-forming climates that persisted as late as <3 Ga (e.g., refs. 2, 4, and 5 and references therein). One hypothesis for reconciling models with data are greenhouse warming by H₂-CO₂ collision-induced absorption (e.g., refs. 6–8). Here, we demonstrate that a different mechanism can explain warm paleoclimates. Recently, warm (\bar{T} ~265 K, where \bar{T} = annual mean temperature) early Mars climates were found in one three-dimensional (3D) global climate model (GCM) simulation of the greenhouse effect of high-altitude water ice clouds (9). However, Urata and Toon (9) did not check for steady-state mass balance for surface H₂O reservoirs, and the high clouds produced by this model require an imposed cloud lifetime, adjusted to be longer than that of Earth clouds by a factor of 10². This and other choices have been described as “not physically reasonable” by subsequent work (10), and other studies also reached similar pessimistic conclusions about the potential of water ice clouds to explain warm paleoclimates (3, 11). For example, Wordsworth et al. (12) found in their model that even if cloud precipitation was (unrealistically) disabled, cloud radiative effects gave only a 1- to 2-y-long rise in surface temperature, too brief to explain geologic data. High clouds are needed for strong cloud warming because high clouds are cold relative to the surface, and the greenhouse-warming

potential of clouds increases when the temperature difference between the cloud-forming altitudes and the surface increases (e.g., refs. 10 and 11). In one-dimensional (1D) models, strong H₂O ice-cloud warming occurs if—and only if—radiatively significant clouds are located at high altitudes (11). Nevertheless, 1D calculations have consistently shown the potential of a tiny quantity of water (just ~0.01 kg/m² H₂O in the form of cloud ice) to raise planet temperature by ~50 K (10, 11). For comparison, Mars today has an average of ~3 × 10⁴ kg/m² of surface H₂O ice and ~0.01 kg/m² atmospheric H₂O vapor. This motivates new 3D simulations in order to understand the discrepant results from earlier studies and test the cloud greenhouse hypothesis. Here, we present cloud greenhouse simulations run from geologically reasonable initial conditions, with physically based cloud microphysics, and run for long enough for the atmosphere to reach equilibrium with surface water reservoirs.

To test the cloud greenhouse hypothesis, we use the MarsWRF GCM (13, 14), modified to include radiatively active water ice clouds. MarsWRF is the Martian implementation of the Planet Weather Research and Forecasting (PlanetWRF) GCM (15), itself derived from the terrestrial Weather Research and Forecasting (WRF) model (16, 17). For early Mars, with static cloud locations, we find maximum warming when cloud optical depth is of order unity and clouds are high (~30 km altitude) (*SI Appendix, Fig. S2*). These 3D results with static clouds are consistent with the 1D results of refs. 10 and 11 (*SI Appendix*). In the remainder of this paper, we use a dynamic water cycle

Significance

Mars is cold today but once had lakes. We evaluated the water ice cloud greenhouse hypothesis for warming early Mars. Our results reconcile previous discrepant results by showing that the cloud greenhouse provides strong warming if the surface has patchy surface H₂O but not if there is very extensive surface H₂O. In our model, arid, warm, stable climates emerge with surface H₂O (and low clouds) only at locations much colder than average surface temperature. At locations horizontally distant from the surface cold traps, clouds are found only at high altitudes, which maximizes cloud warming. As this scenario is consistent with geologic data that suggest a warm, arid early Mars climate, our results support the cloud greenhouse hypothesis for warming early Mars.

Author contributions: E.S.K. and L.J.S. designed research; E.S.K. and L.J.S. performed research; M.A.M. and M.I.R. contributed new reagents/analytic tools; E.S.K. and L.J.S. analyzed data; and E.S.K., L.J.S., and M.A.M. wrote the paper.

The authors declare no competing interest.

This article is a PNAS Direct Submission.

Published under the PNAS license.

¹To whom correspondence may be addressed. Email: kite@uchicago.edu.

²Present address: Jet Propulsion Laboratory, California Institute of Technology, Pasadena, CA 91109.

This article contains supporting information online at <https://www.pnas.org/lookup/suppl/doi:10.1073/pnas.2101959118/-DCSupplemental>.

Published April 26, 2021.

(dynamic clouds), including sedimentation of individual cloud particles, rapid snow-out above an autoconversion threshold, and exchange with surface water ice (*Methods*). We assume that relative humidity is buffered to $\lesssim 1$ by rapid condensation of cloud particles; although air parcels can reach saturation at any temperature in our model, condensation occurs at ≥ 190 K in our output, consistent with our assumption that supersaturation is minor. Individual cloud particles undergo Stokes settling (gas viscosity 10^{-5} Pa s) at a rate set by their modal sizes, with a Cunningham slip correction. Our model has two types of particles: cloud particles that do not fall very fast and snow that does fall fast because the particles are much larger. Cloud particles can be converted to form fast-settling snow if the cloud-particle number density exceeds a threshold. This threshold represents the dependence of cloud-particle coalescence on cloud-particle number density. Specifically, in order to conservatively represent the cloud-depleting effect of mass transfer from slow-settling (cm/s) cloud particles to fast-settling snow (autoconversion), we increase the settling velocity to a fast value (1 m/s) when cloud-particle density exceeds a conservatively low threshold (3×10^{-5} kg/kg). In other words, the conversion of cloud ice to snow does not occur until the number density of cloud particles reaches a certain magnitude. Falling particles either reach the ground as snow or reevaporate when they descend into dry air. Consistent with output from another GCM (11), we find that snow descending into unsaturated air at >30 km will evaporate well before reaching the ground.

Results and Discussion

Cloud Greenhouse Enables Stable, Warm, Arid Climate Consistent with Early Mars Data. With boundary conditions similar to present-day Mars (0.006 bar CO_2 , annual-average H_2O ice-cap temperature <180 K), MarsWRF shows a water cycle with only ~ 10 precipitable μm (pr- μm) of H_2O vapor and only optically thin water ice clouds (*SI Appendix, Fig. S3*) (18), both reminiscent of Mars' spacecraft-era water cycle (*SI Appendix, Fig. S3*). On modern Mars, at low latitudes, water ice clouds are seasonally present at 10- to 40-km altitude (*SI Appendix, Fig. S1*) but have little effect on surface \bar{T} (19). Water ice clouds observed with lidar at high latitudes on modern Mars resemble terrestrial cirrus: peak ice-water content is ~ 1 mg/m³, and fall streaks are directly observed (20).

Our early Mars reference simulation uses Mars Orbiter Laser Altimeter topography, a faint young Sun ($0.8 \times$ modern solar luminosity), a modal cloud-particle radius of 10 μm , and 0.6 bar pCO_2 (*Methods*) (sensitivity tests are described in *SI Appendix*). First, we consider a cold, dry initial condition with surface H_2O (ice) initially restricted to the South Polar region ($>75^\circ\text{S}$) and on high ground (>4 km elevation) at Alba Mons—both relatively cold locations. We describe our model spin-up to show that a stable, warm climate can be reached from a cold, dry start. At first, temperatures are cold ($\bar{T} < 217$ K) with tenuous water ice clouds at altitudes 5 to 20 km. As more water vapor is injected into the atmosphere, surface temperature rises and the condensation level above which clouds can form rises to higher altitude. Water vapor is horizontally well mixed, and clouds occur at all latitudes. $\bar{T} > 260$ K occurs ~ 17 y after the cold/dry start (*SI Appendix, Fig. S4*). After high-altitude clouds become radiatively significant, water vapor continues to build up for a further ~ 20 y, before stabilizing as the surface water ice reservoirs reach steady state (time-average surface relative humidity ~ 1 at the surface cold traps).

Results after the run has reached stable warm-climate steady state ($\bar{T} = 263$ K) in equilibrium with surface water ice are shown in Fig. 1. Water vapor is well mixed horizontally (*SI Appendix, Fig. S5A*), and the global-average cloud water column is 4,000 μm . The warm low latitudes (30°S to 30°N) are humidified by saturated air from the cooler, higher latitudes (as in some endmember models of the climate of Titan; ref. 21). This leads to arid conditions in

the low latitudes, with global-average surface relative humidity of 25% (*SI Appendix, Fig. S5B*). However, saturation is reached at high altitudes in low latitudes, so clouds form. In the low latitudes, peak cloud ice-water content is ~ 1 mg/m³ (less during the day, more during the night) at ~ 25 -km altitude where temperatures are ~ 220 K (*SI Appendix, Fig. S5D*). Essentially, the spatially restricted surface ice distribution, with ice only at relatively cold locations, leads to low global-average surface relative humidity. For lower surface relative humidity (at fixed surface temperature), moisture must be lifted higher to condense and form clouds. These high clouds provide strong warming.

Cloud cover is near global in the GCM after steady state has been reached (*SI Appendix, Fig. S5C*). In our early Mars model, cloud cover is mainly set by the distribution of surface H_2O , instead of (as on Earth) atmospheric circulation and transport processes. This difference can be understood as follows. On modern Earth, the water lifetime in the atmosphere is ~ 10 d. By contrast, in our warm/arid early Mars simulations, the residence time of water substance in the atmosphere is >1 y. The long residence time of water vapor ensures a low-level water vapor mixing ratio that is uniform—to within 20% away from the surface cold traps. Because of this uniformity in $\text{H}_2\text{O}_{(\text{v})}$, away from the surface cold traps, the story of cloud formation is essentially 1D (vertical). The two-order-of-magnitude contrast in atmospheric water lifetime between our early Mars model and modern Earth reduces the importance of the details of transport dynamics/overturning circulation in understanding the distribution of water and why there are clouds at all latitudes and longitudes. (Once formed, cloud particles in our GCM typically move <100 km from their formation locations.) By contrast, Earth's water vapor column abundance varies horizontally by a factor of >60 . The two planets are in different regimes. In our early Mars model, dynamics still matter for explaining locally sharp latitudinal gradients in cloud thickness (Fig. 14). In summary, global cloud cover is enabled by the following attributes of the system (22): 1) atmospheric H_2O has no sink except for the spatially restricted surface cold traps; 2) atmospheric H_2O has a residence time that is longer than the atmospheric mixing time (9); and 3) except at surface cold traps, individual cloud particles do not fall to the surface, instead they sublime just below the cloud base (without being transported far from the cloud) and moisten the subcloud layer. For these reasons, water vapor is horizontally well mixed at near-uniform mixing ratio (kg/kg) (*SI Appendix, Fig. S5A*), and this well-mixed water vapor-bearing layer extends to high altitude, where it condenses as a global “capping” cloud layer. The *SI Appendix* includes a discussion of the differences between our early Mars model and modern Mars observations.

Approximately one-half of incoming sunlight is scattered to the surface at low latitudes, but most upwelling longwave radiation is trapped and reradiated by high, cold clouds. This leads (in concert with positive radiative feedback from $\text{H}_2\text{O}_{(\text{v})}$) to strong warming. The peak cloud-ice mass mixing ratio in our early Mars model is the same as is observed for modern Mars low-latitude clouds (19), but provides much more positive radiative forcing because the early Mars model clouds are more extensive, higher, and more optically thick on average. Convection occurs beneath the clouds, and the associated updrafts help to sustain the clouds. The clouds are in equilibrium with surface water ice at locations where surface relative humidity reaches unity, poleward of 75°S , and also at high ground at 40°N . (Similar results are obtained for alternative spatially restricted water ice distributions.) These surface cold trap locations have $\bar{T} < 245$ K, colder than central Greenland. With ice at these locations, warm steady-state climates result even with cold-atmosphere/cold-surface initial conditions (Fig. 2).

Fig. 1*B* shows the resulting mean annual temperatures. In contrast to previous models that could not generate sustained

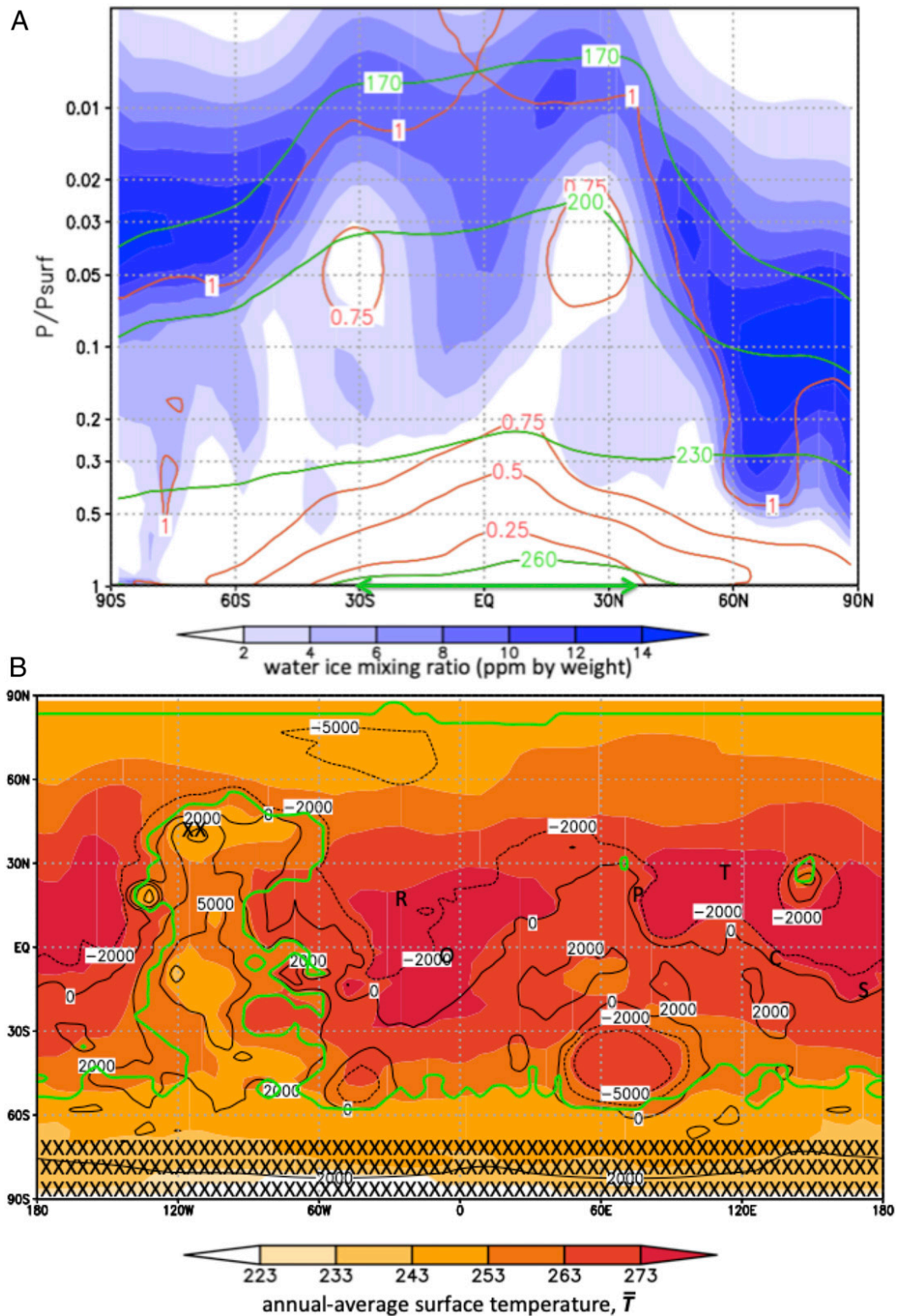


Fig. 1. Results from cloud greenhouse simulation showing warm, arid, stable early Mars climate. This run is for a circular orbit and zero obliquity. (A) Zonally averaged, annual-average output for water ice mixing ratio (ppm by weight, blue shading), atmospheric temperature (K, green contours), and relative humidity (red contours). Y-axis uses terrain-following σ -coordinates ($\sigma = P/P_{\text{surf}}$). Nonzero average ice abundances in areas with average relative humidity < 1 are mostly due to the time/zonal averaging (reference *SI Appendix, Fig. S6D* for a plot of cloud ice-water content, kg/m^3). The green double-headed arrow corresponds to the latitudinal extent of surfaces with $\bar{T} > 273$ K, mapped in B. (B) Annual-average surface temperatures, \bar{T} (K, color shading) and Mars topography (m, black contours) for early Mars simulation in A. "X" marks stable-surface water ice locations. This climate and these water ice locations are stable for centuries or longer, based on extrapolation of vapor-column tendencies. The green contour encloses the very large region that (in a simulation with eccentricity = 0.1 and obliquity = 25° , similar to the orbital parameters of modern Mars) has a continuous 100 sol season with $\bar{T} > 273$ K during every Mars year. Stable, warm, arid climates involve vapor equilibrium with surface ice only at locations much colder than the planet average so that the high altitudes of clouds at locations horizontally distant from the surface cold traps maximize warming. Landing sites are shown for rover missions—(O)ppportunity, (S)pirit, (C)uriosity, (P)erseverance, (T)ianwen-1, and (R)osalind Franklin.

high \bar{T} at +1-km elevations (reviewed in refs. 3 and 5), we find $\bar{T} > 268$ K at almost all known paleolake locations on Mars (almost all are in the 30°S to 30°N band, ref. 1), with $T > 273$ K for many hours each day. This is comfortably warmer than the empirical \bar{T} threshold in the Antarctic Dry Valleys for large perennial ice-covered lakes ($\bar{T} \sim 255$ K, e.g., ref. 23), where seasonal meltwater supply balances evaporative losses. Our GCM does not spatially resolve the deep craters explored by *Curiosity*, *Spirit*, and *Perseverance*, but taking into account the anticorrelation between local elevation and local \bar{T} , our model implies $\bar{T} \geq 273$ K for all rover landing sites (Fig. 1B). This is consistent with the non-detection by rovers of evidence for past ice features. The Fig. 1 simulation is warm but arid ($\sim 25\%$ area-averaged surface relative humidity, *SI Appendix, Fig. S5B*). These results, while different from previous 3D models of melt-permitting climates on Mars, are consistent with geologic data that suggest early Mars had an arid climate (e.g., refs. 24 and 25). In arid climates, lakes could be fed by groundwater flow (24, 26), by infrequent storms associated with mesoscale processes that are not resolved by GCMs (e.g., ref. 27), or transiently by melting of preexisting ice following a cold-to-warm transition (28) (Fig. 3). In our model, low-latitude ground ice (if present) would melt at the onset of the warm climate. This suggests a physical basis for chaos terrain and outflow channel formation (29). The warm, arid climate is strikingly little affected by a test adding $\sim 10^6$ km² of surface H₂O (0.6% of planet area) at the locations of the largest known paleolakes on Mars (1), including *Curiosity*'s field site at Gale (*SI Appendix, Fig. S6B*). In this test, lakes lose H₂O every year, and H₂O is deposited every year on global topographic highs. Ice-cap basal melting and groundwater flow might balance this atmospheric flux and so close this water cycle, as previously hypothesized for early Mars (30, 31) and modern Titan (32). In this case, a warm, arid Mars climate that includes low-latitude groundwater upwelling could self-sustain indefinitely. The cloud greenhouse makes the atmospheric part of this previously hypothesized ancient global water cycle physically self-consistent. More work is needed to test these proposed mechanisms using a hierarchy of models as well as using the geologic record (Fig. 3). Nevertheless, the potential of the Fig. 1 climate to explain geologic data is strong.

Fig. 1 results are for a circular orbit and zero obliquity. Increasing eccentricity to 0.1 and increasing obliquity to 25°, similar to Mars' present-day parameters, causes a 100-d interval with average temperature > 273 K to occur every year in the belt between 40°S and 60°N at all elevations (excepting only Tharsis) (*SI Appendix, Fig. S6A*).

How Spatially Patchy Surface Water Distribution Enables Warm, Stable Climates. We found that the equilibrium climate outcome in our model depends on the initial distribution of surface H₂O. Initial conditions with spatially extensive surface water ice lead to cold climates ($\bar{T} < 220$ K) (*SI Appendix, Fig. S7* and Fig. 2). The cold outcome is counterintuitive in that water vapor is a greenhouse gas, and in Fig. 1 water ice clouds provide strong warming. The cold outcome is not caused by the high albedo of surface water ice. Instead, runs initialized with water ice in warmer-temperature locations (e.g., frozen floodwater in the Northern Lowlands or ice at > 1 -km elevation) yield optically thick, low-lying clouds that produce little or no net warming (*SI Appendix, Figs. S6 and S7*).

As also found by ref. 10, we found cold climates for water ice grain radii ≤ 5 μ m (Fig. 2). Such grains are too small to efficiently absorb upwelling thermal infrared (*SI Appendix, Fig. S8*), and so (as noted by ref. 9) they provide little greenhouse warming (*Methods*).

Why does spatially patchy surface water distribution enable warm climates? Water ice absorbs thermal infrared and forward scatters visible light. Scattering only slowly attenuates downwelling insolation, to an extent set by the total cloud thickness (33). By contrast, absorption exponentially attenuates upwelling long-wave radiation, so (for optically thick clouds) whole-planet energy loss is set by the cloud-top temperature. Cloud-top temperature decreases with altitude following the adiabatic lapse rate, so whole-planet energy loss is minimized (strongest greenhouse) for high-altitude clouds (Fig. 3). Thus, for high-altitude ≥ 10 - μ m-radius clouds, there is a range of cloud optical depths that give strong warming (e.g., refs. 10 and 34). The potential for high-altitude clouds (and strong warming) increases for simulations that have a lower average surface relative humidity. In detail, the average surface relative humidity at steady state depends on many

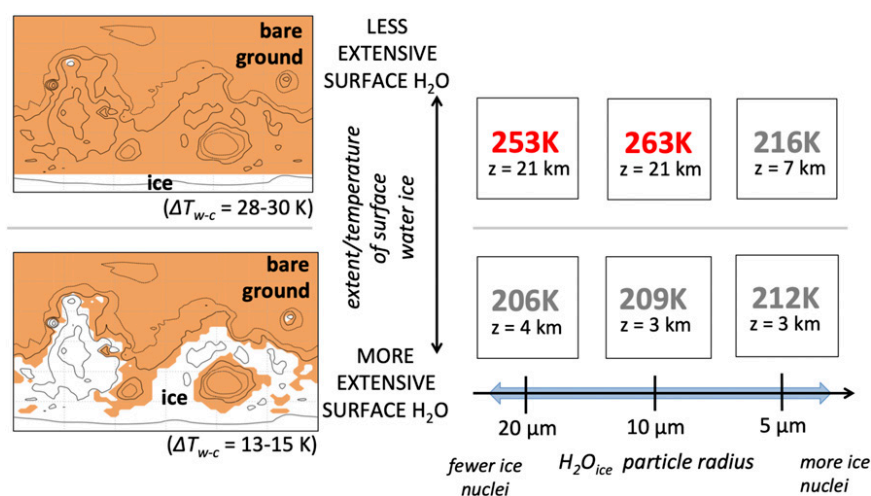


Fig. 2. Control of Mars climate by extent of surface H₂O cover and by ice-cloud particle size. Left column shows ice distribution for each row—white corresponds to surface ice, and ochre corresponds to bare ground (black topography contours are the same as in Fig. 1). ΔT_{w-c} corresponds to the difference (at equilibrium) between the spatial average cold-trap surface temperature and the global average surface temperature. The other columns show (for each run) average temperatures (\bar{T} , in K) and the altitudes of low-latitude (30°S to 30°N) cloud ice water content maxima (z, in km). For example, the 10- μ m run in the top row (Fig. 1) corresponds to a run with fixed cloud particle radius of 10 μ m, and the water ice extent shown in the top map. Warm-climate equilibrated outcomes are shown in red and cold-climate equilibrated outcomes in gray. Results are for cold/dry starts. Double-headed blue arrow corresponds to a wide range of spacecraft-era Mars cloud H₂O_{ice} radii (2 to 70 μ m, ref. 19).

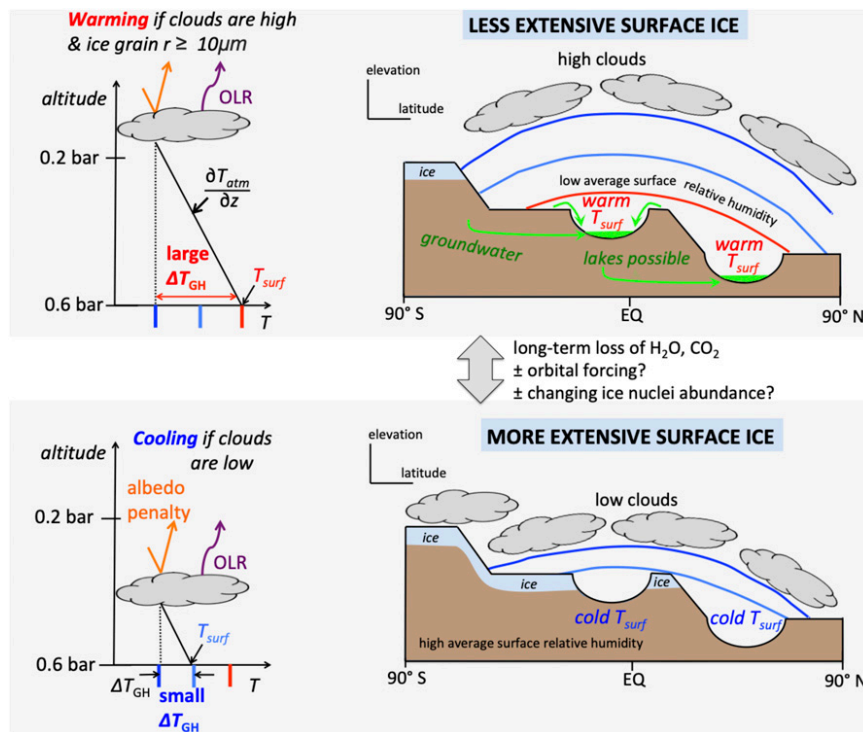


Fig. 3. Cartoon summary of the physical basis for results presented here and possible links to the geologic record of paleolakes and groundwater flow. OLR = Outgoing Longwave Radiation. ΔT_{GH} = temperature difference due to the greenhouse effect. T_{surf} = surface temperature. EQ = equator. On the *Right*, blue lines correspond to cool temperatures, and red lines correspond to warm temperatures.

parameters, including the full two-dimensional initial distribution of surface water ice. Despite this complexity, we have found that a useful index for the GCM runs is the temperature difference (ΔT_{w-c}) between the characteristic temperature of the H_2O -bearing surface (in our model, H_2O ice in surface cold traps), T_c , and the global average temperature, \bar{T} . The absolute humidity of the atmosphere is in effect buffered by the “cold finger” temperature of the surface cold traps, T_c . When the “cold finger” temperature is decreased relative to the typical surface temperature \bar{T} , the typical surface relative humidity goes down. When ΔT_{w-c} is small, the lifting condensation level (LCL, cloud base) is close to the ground, low clouds form, and the cloud greenhouse is weak (Fig. 3). When ΔT_{w-c} is large, low clouds do not form except very close to surface cold traps, and far from the surface cold traps, the LCL is high. As a result, high clouds are possible, and the cloud greenhouse effect can be strong. Overall, the basic physics of scattering, absorption, and the vertical temperature profile cause the optimum in steady-state cloud warming for arid surface conditions (Fig. 3).

For extremely cold planets, there is no longer enough water in the atmosphere to make widespread optically thick clouds, and water cloud warming is negligible. Present-day Mars is in this regime (*SI Appendix*, Figs. S1 and S3). The *SI Appendix* includes a discussion of the differences between our early Mars model and modern Mars observations.

Waxing and Waning of the Cloud Greenhouse over Geologic Time.

Mars’ geologic record shows alternations between wet and dry conditions (e.g., refs. 35 and 36). These alternations might be due to orbital forcing. Alternatively, wet/dry alternations might be due to varying abundance of ice-cloud nuclei (e.g., dust, ash, or meteoric smoke; ref. 37). This is because ice nuclei abundance sets ice grain size, with greater nuclei abundance leading to smaller ice grains. Changes in ice grain size can shift our model between a cold and a warm state (Fig. 2). Our warm-climate model prescribes an ice grain size that is within the observed range for water ice clouds on Mars

today (19). Because we cannot be certain of >3 Ga high-altitude Mars ice nuclei abundance, we cannot be certain that the conditions needed for cloud greenhouse warming occurred on the real early Mars. However, it is also possible that ice nuclei density alternated between values that permitted strong cloud greenhouse warming and values that precluded strong cloud greenhouse warming.

The connection between the distribution of surface H_2O and cloud warming suggests links between Mars’ long-term evolution and the potential for cloud warming. If Mars initially had $>10\times$ the ice-cap H_2O than it does today (e.g., ref. 38), and this H_2O was exposed at the surface in relatively thin ice deposits (e.g., as modeled by ref. 39), then high average surface relative humidity would result, with low clouds, and without strong cloud greenhouse warming (*SI Appendix*, Figs. S6 and S7). As H_2O is lost by escape-to-space, by hydration reactions (mostly irreversible; e.g., ref. 40), and by loss to deep aquifers, or is buried beneath a lag deposit (reversibly; as for Mars’ present-day Planum Australe), the areal extent of surface H_2O may become more spatially restricted. Moreover, as the CO_2 atmosphere thins over time, the temperature difference between the equator and the poles increases, increasing ΔT_{w-c} (however, this is counteracted by reduced CO_2 warming, and it is not clear which effect wins). Moreover, growth of tall volcanoes will create cold ground at high elevation, which may increase ΔT_{w-c} . Each effect can lower the temperature of surface cold traps relative to typical surface temperature, increasing the potential for cloud greenhouse warming (Fig. 1). Thus, Mars’ long-term evolution permits strong cloud greenhouse warming. This is consistent with the geologic evidence for an intensification of aqueous weathering and lake activity ~ 3.7 Ga (41, 42). Further loss of CO_2 (38) and H_2O , and low obliquity (e.g., ref. 43), currently confine Mars to a cold state (*SI Appendix*).

Conclusion

Understanding warm climates on early Mars is difficult. In an early Mars GCM, initialized with a spatially restricted distribution of surface H_2O ice, we find that high-altitude water ice clouds can

give warm annual-mean temperatures. The modeled stable, warm, arid climates are consistent with data that suggest a warm, arid early climate on Mars. Our results support the cloud warming hypothesis (9, 44) as an alternative to the H_2CO_2 collision-induced absorption hypothesis (6–8) for warming early Mars. Our results do not rule out either hypothesis (perhaps both mechanisms contributed), but two tests are imminently possible with rover *Perseverance*. First, in most models of H_2CO_2 collision-induced absorption warming (ref. 7, but see also ref. 45), warming intervals last $\gtrsim 10^5$ y. In the model presented here, warm intervals can last much longer. Therefore, geologic evidence for individually $>10^6$ -y-long warm intervals would favor the cloud greenhouse model. Second, cloud warming can permit lakes on Mars at both high (≥ 0.6 bar) pCO_2 and low pCO_2 (e.g., 0.25 bar, ref. 9) (on Mars, $\text{pCO}_2 \sim$ total atmospheric pressure). In contrast, $\text{pCO}_2 \gtrsim 1$ bar is needed for strong warming by collision-induced absorption (6). Therefore, improved paleo-atmospheric pressure reconstruction using rover observations of pCO_2 -sensitive detrital minerals, constraints on CO_2 escape to space (38), analysis of returned samples, etc. holds out the prospect of understanding the physical basis of habitable climates on early Mars. These results may have implications for understanding habitability in general, because the evidence for warm climates on early Mars is used to define the empirical estimate of the outer edge of the Habitable Zone (46).

Methods

MarsWRF solves the primitive equations using a finite difference methodology on an Arakawa-C grid (47). Both the horizontal and vertical resolution of the model are variable and selectable at run time. Here, a 40-layer vertical grid (from 0 to ~ 100 km) is used, following a modified- σ (terrain-following) coordinate. For the runs shown in Figs. 1 and 2, we have chosen a horizontal resolution of $5.625^\circ \times 3.75^\circ$, which corresponds to a grid of 64 points in longitude \times 48 points in latitude. At this resolution, the model is run with a 3-min dynamical timestep. The Mars orbital state (obliquity, eccentricity, and solar longitude of perihelion) is defined at runtime, along with the prescribed solar luminosity.

A multigas, two-stream radiation code, loosely based on the structure outlined in ref. 48, but modified to use the k -distribution radiative transfer method, is employed in MarsWRF. This method retains much of the accuracy of line-by-line calculations but is significantly faster (e.g., refs. 49 and 50). Information about the particular implementation of the correlated- k method that is used here may be found in ref. 51. Radiative transfer calculations for both gas and aerosol are performed for 14 discrete wavelength bins covering the ultraviolet, visible, and infrared portions of the spectrum (from 0.24 to 1,000 μm). In the present study, dust, CO_2 ice, and water ice aerosols are considered.

Within a single model layer, and for each grid point, the wavelength-dependent opacity from water ice aerosols is determined first for a reference wavelength of 0.67 μm using refractive index data for water ice at 210 K from ref. 52 (*SI Appendix, Fig. S8*). Opacities at other wavelengths are scaled relative to this reference value by the ratio of the extinction cross-sections at 0.67 μm and the other wavelength. As the data from ref. 52 is of higher resolution than the spectral bins within MarsWRF, a weighted average of all calculated opacities within each of the 14 spectral bins is used. Microphysical processes (including sedimentation, cloud formation, and surface deposition) are updated each dynamical timestep, while radiative effects of both gas and aerosol are calculated less frequently (every 30 min). Because CO_2 absorbs around 15 μm , Mars' surface cools mainly by emission through windows in the CO_2 absorption spectrum at ~ 20 μm and at 8 to 12 μm . For the purpose of absorbing light at these wavelengths, the volume-normalized extinction cross-section varies strongly with water ice cloud particle radius (*SI Appendix, Fig. S8*). Water ice cloud particle radii are affected by the number density of ice nuclei (fewer ice nuclei implies bigger water ice particles). The number density of ice nuclei on early Mars depends in part on the capacity of surface aeolian processes to loft dust and on the availability of liftable dust at the surface. In turn, the availability of liftable dust at the surface depends on the long-term balance between dust-aerosol production by wind erosion versus dust-aerosol consumption via sediment induction, and is unknown. To take account of this unknown, we considered modal water ice cloud particle radii (each defining the center of a log-normal distribution) of 5, 10, and 20 μm (Fig. 2). Current Mars water ice particle radii are stated by ref. 19 to be 2 to 5 μm for low-latitude clouds

(e.g., the aphelion cloud belt) and up to 70 μm for high-latitude clouds. Only ice clouds (not mixed-phase clouds) are considered, which is reasonable because most clouds form and reside at <240 K.

Surface material properties were set to Mars-average values similar to those used in other studies (e.g., ref. 53): specifically, thermal inertia is constant ($250 \text{ J m}^{-2} \text{ K}^{-1} \text{ s}^{-1/2}$) and surface albedo is set to 0.2, except in locations where substantial water ice exists, for which surface albedo is set to 0.45. CO_2 condensation is permitted to occur in the model; however, to keep the results easy to interpret we chose boundary conditions and initial conditions (mainly CO_2 pressure) for which CO_2 condensation in the model is initially unimportant. The initial atmospheric and surface temperatures are set to be warm enough that runaway atmospheric collapse does not initiate during model spin-up (e.g., for the run in Fig. 1, global average initial temperatures are 239 K for the surface and 211 K for the near-surface atmosphere).

Water Cycle Surface Boundary Condition. A large surface water ice source is prescribed at $t = 0$; the location of the source varies between runs. During the run, the location of the surface water ice can shift. The model uses a basic water cycle in which water vapor and ice mass mixing ratios (kg/kg) are transported as tracers in the atmosphere. If the water vapor concentration in a grid box exceeds saturation, the excess vapor is converted to ice. Water can exchange between the atmosphere and surface in two ways: 1) water can be deposited onto the surface due to the sedimentation of ice particles, with the sedimentation velocity calculated using Stokes' law modified with a Cunningham slip-flow correction factor (54); and 2) additionally, water vapor can condense onto the surface, or water ice can sublime from the surface (if surface water ice is locally available), depending on the humidity gradient between the surface and lowest model layer. In this case, the flux of water is given by the following:

$$F = \rho u C_d (q_{\text{sat}} - q_v), \quad [1]$$

where ρ , u , and q_v are the atmospheric density, wind speed, and water vapor mass mixing ratio in the lowest model layer, and q_{sat} is the saturation vapor mass mixing ratio at the ground. C_d is a drag coefficient given by the following:

$$C_d = [\kappa / \ln(z/z_0)]^2, \quad [2]$$

where $\kappa = 0.4$ is the Von Kármán constant, z is the midpoint height of the lowest model layer, and z_0 is the surface roughness. The sublimation and deposition of ice affects the surface temperature through latent heat effects, given by the following:

$$H = -L_{\text{sub}}(\Delta m_i / \Delta t), \quad [3]$$

where $L_{\text{sub}} = 2.83 \times 10^6 \text{ J kg}^{-1}$ is the latent heat of sublimation of ice, Δm_i is the change in mass per unit area of surface ice, and Δt is the model time step.

Water ice clouds in the model are radiatively active. The ice mass mixing ratio in each grid box is converted to an opacity via the following:

$$\tau = \text{tnq} \times 0.00 \text{ be}; (Q_{\text{ext}} q_i dp) / (g \rho_i r_{\text{eff}}), \quad [4]$$

where q_i is the ice mass mixing ratio, ρ_i and r_{eff} are the density and effective radius of the ice particles, Q_{ext} is the extinction coefficient of ice (*SI Appendix, Fig. S8*), g is the mean acceleration due to gravity, and dp is the vertical pressure difference over the grid box (cf. ref. 55).

H_2O Ice-Cloud Formation. We assume that relative humidity is buffered to $\lesssim 1$ by rapid condensation of cloud particles. In our model output, air parcels reach saturation at $\gtrsim 190$ K. Supersaturation is neglected; supersaturation would lead to cloud particle formation at greater heights, which is associated with even stronger greenhouse warming (10, 11).

H_2O Ice-Cloud Particle Destruction: Order-of-Magnitude Reasoning. For ice mixing ratio 10^{-5} kg/kg at 3 kPa and 200 K, the ice concentration is about $4 \times 10^{-7} \text{ kg/m}^3$, which (for particle radius 10 μm) gives a particle number density of $\sim 1 \text{ cm}^{-3}$. The corresponding lifetime of 10- μm -diameter particles against Brownian coagulation is years or longer (56), neglecting order-unity corrections for van der Waals, Coulomb, and hydrodynamic forces. To estimate the timescale for coagulation from gravitational settling, suppose that particles move relative to each other at the Stokes settling speed ($u_s < 1 \text{ cm/s}$). This timescale is about $1/(10^{-4} \text{ m}^{-1} u_s)$ where 10^{-4} m^{-1} is the optical depth per meter; that is, this timescale is weeks or longer. Since these timescales are all long compared to air-parcel vertical velocity timescales, the cloud particles are usually destroyed by encountering unsaturated air, for example, by settling. Snow settling into unsaturated air at >30 km will evaporate well before

reaching the ground (11, 57). The short timescale for sublimation has been noted for modern Mars (58).

Definition of Steady State. MarsWRF conserves total H₂O mass (vapor + surface ice + cloud ice) to better than 0.0002% y⁻¹. In equilibrated runs, we see drift of +0.15% y⁻¹ in atmospheric vapor mass. Because the drift is much smaller than the water vapor tendencies during model spin-up (SI Appendix, Fig. S4), we interpret the drift as due to a combination of model resolution effects and climatological noise, rather than a harbinger of a physical instability. Even if this drift adds up over time (which we do not consider likely), then the climate would remain warm for centuries.

Tests. In order to check our model, we first imposed cloud altitude, optical thickness, and particle size and varied these parameters in order to reproduce the results of ref.

10 (SI Appendix, Fig. S2 and Supplementary Text). Next, we allowed dynamic clouds and ran with boundary conditions similar to modern Mars, finding a water ice cycle that is reminiscent of the observed modern Mars one (SI Appendix, Fig. S3 and Supplementary Text). Further sensitivity tests are shown in SI Appendix, Fig. S6.

Data Availability. Model output data have been deposited in Figshare (https://figshare.com/articles/dataset/wrfout_d01_0036-00009_20_00_00/14182643/1).

ACKNOWLEDGMENTS. We thank two anonymous reviewers for useful reviews, M. Turbet and B. Fan for discussions, and C. Lee for MarsWRF assistance. We acknowledge use of the University of Chicago Research Computing Center resources. A portion of this work was performed at the Jet Propulsion Laboratory under contract with NASA. Grants were received from NASA (NNX16AG55G and NNX15AH98G).

- C. I. Fassett, J. W. Head, Valley network-fed, open-basin lakes on Mars: Distribution and implications for Noachian surface and subsurface hydrology. *Icarus* **198**, 37–56 (2008).
- J. P. Grotzinger *et al.*, A habitable fluvio-lacustrine environment at Yellowknife Bay, Gale crater, Mars. *Science* **343**, 1242777 (2014).
- R. D. Wordsworth, The climate of early Mars. *Annu. Rev. Earth Planet. Sci.* **44**, 381–408 (2016).
- R. M. Haberle, D. C. Catling, M. H. Carr, K. J. Zahnle, “The early Mars climate system” in *The Atmosphere and Climate of Mars*, R. M. Haberle *et al.*, Eds. (Cambridge University Press, 2017), pp. 497–525.
- E. S. Kite, Geologic constraints on early Mars climate. *Space Sci. Rev.* **215**, 10 (2019).
- M. Turbet, C. Boulet, T. Karman, Measurements and semi-empirical calculations of CO₂ + CH₄ and CO₂ + H₂ collision-induced absorption across a wide range of wavelengths and temperatures. Application for the prediction of early Mars surface temperature. *Icarus* **346**, 113762 (2020).
- R. Wordsworth *et al.*, Transient reducing greenhouse warming on early Mars. *Geophys. Res. Lett.* **44**, 665–671 (2017).
- R. M. Ramirez *et al.*, Warming early Mars with CO₂ and H₂. *Nat. Geosci.* **7**, 59–63 (2014).
- R. A. Urata, O. B. Toon, Simulations of the martian hydrologic cycle with a general circulation model: Implications for the ancient martian climate. *Icarus* **226**, 229–250 (2013).
- R. M. Ramirez, J. F. Kasting, Could cirrus clouds have warmed early Mars? *Icarus* **281**, 248–261 (2017).
- M. Turbet *et al.*, The environmental effects of very large bolide impacts on early Mars explored with a hierarchy of numerical models. *Icarus* **335**, 113419 (2019).
- R. Wordsworth *et al.*, Global modelling of the early martian climate under a denser CO₂ atmosphere: Water cycle and ice evolution. *Icarus* **222**, 1–19 (2013).
- A. D. Toigo, C. Lee, C. E. Newman, M. I. Richardson, The impact of resolution on the dynamics of the martian global atmosphere: Varying resolution studies with the MarsWRF GCM. *Icarus* **221**, 276–288 (2012).
- M. A. Mischna, V. Baker, R. Milliken, R. Richardson, C. Lee, Effects of obliquity and water vapor/trace gas greenhouses in the early martian climate. *J. Geophys. Res.* **118**, 560–576 (2013).
- M. I. Richardson, A. D. Toigo, C. E. Newman, PlanetWRF: A general purpose, local to global numerical model for planetary atmospheric and climate dynamics. *J. Geophys. Res.* **112**, E09001 (2007).
- W. C. Skamarock, J. B. Klemp, A time-split nonhydrostatic atmospheric model for weather research and forecasting applications. *J. Comput. Phys.* **227**, 3465–3485 (2008).
- J. G. Powers *et al.*, The Weather Research and Forecasting model: Overview, system efforts, and future directions. *Bull. Am. Meteorol. Soc.* **98**, 1717–1737 (2017).
- C. Lee, M. I. Richardson, C. E. Newman, M. A. Mischna, The sensitivity of solsticial pauses to atmospheric ice and dust in the MarsWRF general circulation model. *Icarus* **311**, 23–34 (2018).
- R. T. Clancy *et al.*, “Clouds” in *The Atmosphere and Climate of Mars*, R. M. Haberle *et al.*, Eds. (Cambridge University Press, 2017), pp. 42–75.
- C. Dickinson *et al.*, Lidar atmospheric measurements on Mars and Earth. *Planet. Space Sci.* **59**, 942–951 (2011).
- C. Griffith *et al.*, “Storms, clouds, and weather” in *Titan: Interior, Surface, Atmosphere, and Space Environment*, I. Müller-Wodarg, C. A. Griffith, E. Lellouch, T. E. Cravens, Eds. (Cambridge University Press, Cambridge, UK, 2014), pp. 190–223.
- J. T. Bartlett, G. E. Hunt, Venus cloud cover. *Nature Phys. Sci.* **238**, 11–12 (1972).
- C. P. McKay, “Polar lakes, streams, and springs as analogs for the hydrological cycle on Mars” in *Water on Mars and Life*, T. Tokano, Ed. (Springer, Berlin, 2005), pp. 219–233.
- J. C. Andrews-Hanna, R. J. Phillips, M. T. Zuber, Meridiani Planum and the global hydrology of Mars. *Nature* **446**, 163–166 (2007).
- R. M. Ramirez, R. A. Craddock, The geological and climatological case for a warmer and wetter early Mars. *Nat. Geosci.* **11**, 230–237 (2018).
- D. G. Horvath, J. C. Andrews-Hanna, Reconstructing the past climate at Gale crater, Mars, from hydrological modeling of late-stage lakes. *Geophys. Res. Lett.* **44**, 8196–8204 (2017).
- K. E. Scanlon, J. W. Head, J.-B. Madeleine, R. D. Wordsworth, F. Forget, Orographic precipitation in valley network headwaters: Constraints on the ancient Martian atmosphere. *Geophys. Res. Lett.* **40**, 4182–4187 (2013).
- S. A. Wilson, A. D. Howard, J. M. Moore, J. A. Grant, A cold-wet middle-latitude environment on Mars during the Hesperian-Archean transition: Evidence from northern Arabia valleys and paleolakes. *J. Geophys. Res.* **121**, 1667–1694 (2016).
- T. E. Zegers, J. H. P. Oosthoek, A. P. Rossi, J. K. Blom, S. Schumacher, Melt and collapse of buried water ice: An alternative hypothesis for the formation of chaotic terrains on Mars. *Earth Planet. Sci. Lett.* **297**, 496–504 (2010).
- S. M. Clifford, T. J. Parker, The evolution of the martian hydrosphere: Implications for the fate of a primordial ocean and the current state of the northern plains. *Icarus* **154**, 40–79 (2001).
- J. C. Andrews-Hanna, K. W. Lewis, Early Mars hydrology: 2. Hydrological evolution in the Noachian and Hesperian epochs. *J. Geophys. Res.* **116**, E02007 (2011).
- S. P. Faulk, J. M. Lora, J. L. Mitchell, P. C. D. Milly, Titan’s climate patterns and surface methane distribution due to the coupling of land hydrology and atmosphere. *Nat. Astron.* **4**, 390–398 (2020).
- R. Pierrehumbert, *Principles of Planetary Climate* (Cambridge University Press, 2010).
- C. Goldblatt, K. Zahnle, Clouds and the faint young Sun paradox. *Clim. Past* **7**, 203–220 (2011).
- J. M. Metz *et al.*, Sulfate-rich eolian and wet interdune deposits, Erebus crater, Mars. *J. Sediment. Res.* **79**, 247–264 (2009).
- R. M. E. Williams, C. M. Weitz, Reconstructing the aqueous history within the southwestern Melas basin, Mars: Clues from stratigraphic and morphometric analyses of fans. *Icarus* **242**, 19–37 (2014).
- V. L. Hartwick, O. B. Toon, N. G. Heavens, High-altitude water ice cloud formation on Mars controlled by interplanetary dust particles. *Nat. Geosci.* **12**, 516–521 (2019).
- B. M. Jakosky *et al.*, Loss of the martian atmosphere to space: Present-day loss rates determined from MAVEN observations and integrated loss through time. *Icarus* **315**, 146–157 (2018).
- J. L. Fastook, J. W. Head, Glaciation in the Late Noachian Icy Highlands: Ice accumulation, distribution, flow rates, basal melting, and top-down melting rates and patterns. *Planet. Space Sci.* **106**, 82–98 (2015).
- J. Mustard, “Sequestration of volatiles in the martian crust through hydrated minerals: A significant planetary reservoir of water” in *Volatiles in the Martian Crust*, J. Filiberto, S. Schwenzer, Eds. (Elsevier, 2018), pp. 247–263.
- A. D. Howard, J. M. Moore, R. P. Irwin, An intense terminal epoch of widespread fluvial activity on early Mars: 1. Valley network incision and associated deposits. *J. Geophys. Res.* **110**, E12514 (2005).
- J. Carter, D. Loizeau, N. Mangold, F. Poulet, J.-P. Bibring, Widespread surface weathering on early Mars: A case for a warmer and wetter climate. *Icarus* **248**, 373–382 (2015).
- J.-B. Madeleine *et al.*, Recent ice ages on Mars: The role of radiatively active clouds and cloud microphysics. *Geophys. Res. Lett.* **41**, 4873–4879 (2014).
- T. L. Segura, O. B. Toon, A. Colaprete, Modeling the environmental effects of moderate-sized impacts on Mars. *J. Geophys. Res.* **113**, E11007 (2008).
- R. M. Ramirez, A warmer and wetter solution for early Mars and the challenges with transient warming. *Icarus* **297**, 71–82 (2017).
- R. K. Kopparapu *et al.*, Habitable zones around main-sequence stars: New estimates. *Astrophys. J.* **765**, 131 (2013).
- A. Arakawa, V. R. Lamb, Computational design of the basic dynamical processes of the UCLA general circulation model. *Methods Comput. Phys.* **17**, 173–265 (1977).
- J. M. Edwards, A. Slingo, Studies with a flexible new radiation code, I: Choosing a configuration for a large-scale model. *Q. J. R. Meteorol. Soc.* **122**, 689–719 (1996).
- A. A. Lacis, V. Oinas, A description of the correlated *k* distribution method for modeling nongray gaseous absorption, thermal emission, and multiple scattering in vertically inhomogeneous atmospheres. *J. Geophys. Res.* **96**, 9027–9074 (1991).
- Q. Fu, K. N. Liou, On the correlated *k*-distribution method for radiative transfer in nonhomogeneous atmospheres. *J. Atmos. Sci.* **49**, 2139–2156 (1992).
- M. A. Mischna, C. Lee, M. Richardson, Development of a fast, accurate radiative transfer model for the Martian atmosphere, past and present. *J. Geophys. Res.* **117**, E10009 (2012).
- H. Iwabuchi, P. Yang, Temperature dependence of ice optical constants: Implications for simulating the single-scattering properties of cold ice clouds. *J. Quant. Spect. Rad. Trans.* **112**, 2520–2525 (2011).
- E. S. Kite, I. Halevy, M. A. Kahre, M. Manga, M. Wolff, Seasonal melting and the formation of sedimentary rocks on Mars. *Icarus* **223**, 181–210 (2013).
- W. B. Rossow, Cloud microphysics: Analysis of the clouds of Earth, Venus, Mars, and Jupiter. *Icarus* **36**, 1–50 (1978).
- F. Forget, F. Hourdin, O. Talagrand, CO₂ Snowfall on Mars: Simulation with a general circulation model. *Icarus* **131**, 302–316 (1998).
- J. Seinfeld, S. Pandis, *Atmospheric Physics and Chemistry* (Wiley, ed. 3, 2016).
- D. Gregory, A consistent treatment of the evaporation of rain and snow for use in large-scale models. *Mon. Weather Rev.* **123**, 2716–2732 (1995).
- D. V. Michelangeli, O. B. Toon, R. M. Haberle, J. B. Pollack, Numerical simulations of the formation and evolution of water ice clouds in the martian atmosphere. *Icarus* **102**, 261–285 (1993).

Supplementary Text.

Comparison of GCM output to previous studies and to the modern Mars climate.

The runs described in the main text have fully dynamic water ice clouds. Previous studies have investigated the early Mars cloud greenhouse hypothesis using 1D models with cloud layers of prescribed/imposed thickness and altitude (1, 2). In order to allow comparison of our 3D model to the previous 1D results, we carried out simulations to study the effect of a global cloud layer of prescribed/imposed thickness and altitude on ancient Mars surface temperature – using a 3D model to simulate a 1D effect. For these fixed-cloud-layer comparison runs only (not for the fully dynamic runs reported in the main text), we performed 3D simulations using MarsWRF at a resolution of 7.5° in latitude and longitude with 40 vertical levels extending up to around 100 km. Surface thermal inertia and bare ground albedo are set to globally-constant values of $250 \text{ J m}^{-2} \text{ K}^{-1} \text{ s}^{-1/2}$ and 0.2, respectively. Present-day topography derived from MOLA data is used, and the atmosphere has a mean surface pressure of 1 bar. The radiative impact of dust is not included, in order to isolate the effects of water ice clouds.

Ninety different comparison simulations were run. The simulations varied in the pressure at the center of the single cloud layer (varied from 0.5-0.001 bar, i.e. around 8-70 km), and in the cloud optical depth (at $0.67 \mu\text{m}$; varied from 0.5-7). Due to the variable spacing of model layers, clouds at 8 km altitude are around 2 km thick, and clouds at 70 km altitude are around 3.5 km thick. The results are shown in Fig. S2. As the optical depth of clouds increases, the amount of shortwave radiation reaching the surface decreases, but the ability of the cloud to absorb and re-emit upwelling longwave radiation increases. In our simulations, the warmest surface temperatures occur for clouds with visible optical depths of around 4.5-6. For smaller optical depths the thinner clouds are not as efficient at absorbing and re-emitting the upwelling longwave radiation, and for greater optical depths the reduction in shortwave radiation reaching the surface limits surface warming. As the altitude of the cloud layer decreases, the clouds are located at increasingly warmer temperatures. As such, the temperature difference between the surface and cloud layer decreases, and hence the ability of the cloud to modify the upwelling longwave radiation decreases. A similar phenomenon is observed on present-day Mars, where thick polar hood H_2O clouds close to the surface have little radiative impact, but thinner H_2O clouds at higher altitudes in the tropics can have larger radiative impacts (3). In our simulations, the warmest surface temperatures occur for clouds located at pressures of around 0.06-0.02 bar (30-40 km). Ref. 1 performed 1D modeling studies of a 0.5 bar atmosphere, with a 1 km cloud deck composed of $10\text{-}\mu\text{m}$ ice particles. They found that the greatest surface warming occurred for clouds centered at 0.056 bar, and for optical depths between 2.78 and 8.42. These values are in agreement with the range of optical depths and pressures for which our simulations produce peak warming (Figure S2a,c). Ref. 1 also found that peak warming in a 1 bar atmosphere occurred for clouds centered at around 0.15 bar. However, ref. 2 reproduced the ref. 1 atmosphere simulations for 1 bar atmospheric pressure with increased vertical resolution, and found peak warming actually occurs at an altitude of around 0.02 bar for $10\text{-}\mu\text{m}$ ice particles, in agreement with our results at 0.5 bar, and those of ref. 5.

Taking the cloud height and optical depth that gave peak warming, we then performed 45 additional simulations with a cloud layer centered at 0.03 bar with an optical depth of 5.

In these simulations we varied the obliquity from 15-55°, and the solar longitude of perihelion across all seasons. The results are also shown in Fig. S2 (panels b and d). In terms of average surface temperatures there is only 10 K difference across all the simulations, but peak temperatures vary by 30 K. It is clear that peak temperatures increase as the obliquity increases, due to increased warming of the northern hemisphere atmosphere, which is thicker due to its lower elevation. For a similar reason, the coldest temperatures occur when the obliquity is low and perihelion corresponds to southern hemisphere summer.

In order to test the model's behavior when simulating the radiative impact of water ice clouds in a thin atmosphere (~0.006 bar surface pressure, corresponding to present day Mars surface pressure), we performed two simulations with MarsWRF at a resolution of 5° in latitude and longitude with 40 vertical levels extending up to around 100 km. MarsWRF has previously been shown to capture the global temperature structure and water cycle observed in the present-day atmosphere (6-7). On more local scales, MarsWRF also captures well entry, descent and landing profiles (8-9), and the diurnal and seasonal cycles of pressure, temperature, wind and thermal tides from the *Curiosity* rover at Gale crater (10-12). The simulations performed here are not intended to match a specific Mars year, but to highlight the changes caused by the radiative impact of clouds. Surface thermal inertia, bare ground albedo, topography and orbital parameters were set to present-day values, and a permanent north polar ice cap was defined poleward of 80°N. (A north polar ice cap is unstable at 0.6 bar pCO₂, because the north polar region is topographically low-lying and low-lying regions are warm at high pCO₂). Atmospheric ice is formed whenever the water content of a grid box exceeds saturation, with ice particles having a log-normal distribution with an effective radius of 5 µm. For these test simulations, autoconversion was switched off, which is reasonable because cloud densities in the present-day hyper-arid Mars climate are low (Fig. S3). The radiative effect of dust was included, but the dust optical depth was set to a constant value of 0.1 (on the low end of observed values for spacecraft-era aphelion season), with a Conrath profile in the vertical.

Fig. S3 shows the results from year 10 of the simulations at four different seasons. Considering first aphelion season (Fig. S3a-f), the inclusion of radiatively-active water ice clouds drastically improves the agreement with Mars Climate Sounder (MCS) data. When clouds are radiatively inactive (Fig. S3a,d), temperatures in the tropics are ~20 K cooler than the observed values at ~20-50 km altitude, but this is reduced to an error of only ~2-5 K when clouds are radiatively active (Fig. S3b,e). There is also an improvement in the representation of the polar vortices. In the simulations with radiatively-active clouds, the near-surface temperatures are reduced and the polar warmings – the regions of warmer temperatures above the vortices – are strengthened. However, the polar vortices are significantly affected by dust in the atmosphere, both in terms of the opacity and the vertical distribution (e.g., 13-14). As such, these simulations with a constant dust distribution cannot represent the true vortex structure. During perihelion season (Fig. S3g-l) the temperature of the atmosphere increases due to stronger insolation and dust storm activity. Again, our constant dust distribution cannot represent this temperature increase, but it is clear that cloud radiative effects still improve the model's temperature structure. The clouds increase temperatures in the tropical middle atmosphere by ~15 K, which reduces the difference between the MCS observations from around -20-25 K to around -5-10 K. The additional warming required, particularly in the lower atmosphere, is due to the lower dust abundance in the model. The improvement to the polar vortex structure at southern hemisphere

summer solstice (Fig. S3j-l) is also notable. The largest change to surface temperatures from cloud radiation is during northern hemisphere summer solstice (Fig. S3df), when the subliming north polar ice cap produces an optically thick aphelion cloud belt (15). At this time, the nighttime surface temperatures in the simulation with radiatively-active water ice clouds are up to 8 K warmer. The largest warming occurs over Tharsis and Arabia Terra, where the thickest clouds form.

The increased temperatures at all seasons, particularly in the tropics, results in clouds moving to higher altitudes, and becoming more in agreement with the cloud locations in the MCS data. In general, the water ice mass mixing ratios in the simulations are larger than those in the MCS data. We obtain the ice mass mixing ratios from the MCS data following the procedure in ref. 16. However, there are numerous issues when performing this calculation. Firstly, the aerosol opacity and temperature errors increase both low and high in the atmosphere (17), limiting the region of useful data to ~ 1 -100 Pa. Secondly, MCS retrievals cannot observe the most optically thick clouds, and so will be slightly biased to lower values. Lastly, conversion from opacities to mass mixing ratios requires knowledge of the water ice particle effective radius and extinction coefficient. As such, the water ice mass mixing ratios in Fig. S3c,f,i and k should not be taken as exact, but as a lower limit on likely values.

All Global Climate Models, including MarsWRF, have energy imbalances due to finite model resolution, rounding errors, etc. The energy imbalances in our 0.006 bar runs are $< 0.2 \text{ W/m}^2$. The high- $p\text{CO}_2$ control runs discussed earlier in this subsection, but not the “production” runs described in the main text and elsewhere in this Supplementary Information, have an energy imbalance at steady state of up to 5 W/m^2 . In all of our warm-climate runs, after temperature and water vapor concentrations have stabilized (Figure S4), the top-of-atmosphere energy imbalance is $\leq 1.7 \text{ W/m}^2$, i.e. $\leq 1.5\%$ of Early Mars planet-averaged insolation. The contribution of ground conduction / geothermal heating to the energy budget is $< 0.1 \text{ W/m}^2$. Therefore, energy imbalance does not affect the conclusions of this study.

Supplementary discussion of early Mars GCM output.

To show that our warm climate (Fig. 1) is consistent with Mars rover data, we added perennial reservoirs of H_2O of area $\sim 10^5 \text{ km}^2$ centered near the location of Gale crater, and also a $\sim 5 \times 10^5 \text{ km}^2$ sea in Eridania, as well as $\sim 10^5 \text{ km}^2$ lakes at Gale, Antoniadi, Cassini, and Tikhonravov (total area $\sim 10^6 \text{ km}^2$) (18) to a warm climate. Some of these lakes are predicted by the model (Fig. S6b) to be ice covered, and others are predicted by the model to be open-water lakes. Our model does not realistically treat water vapor fluxes from open-water liquid lakes (these are modeled as warm pseudo-ice blocks); thus, this test run does not realistically represent the actual water vapor fluxes from open-water perennial lakes of 10^6 km^2 in cumulative area. Nevertheless, the run is the best proxy for lakes that is possible with the current configuration of MarsWRF. In future, it might be interesting to add explicit treatment of liquid water and rainfall to MarsWRF (as well as mesoscale modeling of cloud processes). For the just-described additional-equatorial-vapor-injection run, we find only minor climate perturbation ($\sim 1 \text{ K}$ warming) from the pre-lake-injection warm climate. This is because the $\sim 50\%$ increase in column $\text{H}_2\text{O}_{(v)}$ is fully counterbalanced by the higher albedo of thicker H_2O ice clouds. The annual net water vapor flux from the lakes is routed to the polar and volcano-

summit surface cold traps. (If the perennial reservoirs of H₂O at lake locations are added from a cold/dry start, which is geologically unrealistic because lakes require warm temperatures, then, even if there are no other surface H₂O sources, a cold climate results).

If average surface relative humidity controls cloud-base temperature (relative to the surface temperature), but the strength of the cloud effect on upwelling longwave radiation (greenhouse effect) is set by cloud-top temperature, why does low average surface relative humidity enable strong warming? Suppose that the surface relative humidity is high, and the cloud-top altitude is also high. In that case, the cloud will likely be optically thick as well as physically thick, and the albedo increase will defeat the strong warming (Fig. S2). Why is this? For a cloud with an optical depth of more than a few, warming saturates (the OLR will not be less than the emission at the cloud-top temperature). However, the albedo penalty continues to increase, due to the sigmoidal form of the scattering equation plus the strong forward scattering in the visible of big ice crystals (19, 20). (The grain-size dependent ratio of extinction efficiency in the infrared to extinction efficiency in the visible also contributes). Thus, strong cloud warming is only possible when cloud-top altitude is high and the cloud is not too optically thick (1, 2) (Fig. S2). These conditions are enabled by low average surface relative humidity.

For a dry start with extensive surface water ice at relatively warm surface locations, as the water vapor mixing ratio rises from an initially small value, the cloud base will initially be at very high altitude (forming clouds that warm the surface) and later the cloud base will move to lower altitudes (allowing the formation of clouds that cool the surface). This predicts a short burst of warmth (seen in many of our cold-outcome simulations, and also reported by ref. 21), which fails to match geologic data for early Mars lakes.

Supplementary discussion of geologic boundary conditions.

As discussed in the main text, there are many ways to vary ΔT_{w-c} . ΔT_{w-c} is connected to the area-averaged surface relative humidity. To illustrate using endmember examples, if ice covers the entire surface, then ΔT_{w-c} is zero, and area-averaged surface relative humidity will be >50%. On the other hand, if ice is found only at a mountain summit that is much colder than the rest of the planet, then ΔT_{w-c} is large, and the climate will be arid. We now provide more background on one specific mechanism for varying ΔT_{w-c} : formation of sublimation lag deposits (Fig. S9). Sublimation lag deposits set the intensity of the water cycle on today's Mars. On Mars in the spacecraft era, there is an exposed perennial H₂O ice cap near the North Pole (water ice volume $\sim 10^6$ km³), a sublimation-lag-covered H₂O-ice-dominated deposit near the South Pole (water ice volume $\sim 10^6$ km³), and lag-deposit-covered glaciers at midlatitudes (water ice volume $> 10^5$ km³; ref. 22). Although the sublimation lag covers are generally <10 m thick, it is sufficient to isolate the voluminous non-North-Pole water ice deposits from Mars' annual water cycle (Fig. S9) (see ref. 23 for theoretical background). Theoretically, sublimation lags could wax and wane due to changes in orbital eccentricity, season of perihelion, and the obliquity of the spin axis, etc. (e.g., 24-25). Sublimation lag deposit growth and shrinkage has likely occurred repeatedly on Mars, which would have had major effects on the distribution of surface-exposed water ice on Mars (26). Thus, sublimation lag deposit growth and shrinkage is a plausible geologic mechanism for variations with time in position on the y-axis in Fig. 2, i.e., in the extent of surface-exposed water ice deposits.

Why water ice clouds on modern Mars do not enable a warm climate.

Our results show that a spatially restricted distribution of surface H₂O (with most surface H₂O significantly colder than planet average temperature) is more favorable for warm climates than is very extensive surface water ice. However, this effect has limits. If the cold-trap temperature is so low that the atmosphere is too dry to form extensive optically thick ice clouds, then strong warming from a water ice cloud greenhouse effect is not possible. Spacecraft-era Mars is in this hyper-arid regime. On today's Mars (25° obliquity, $p_{\text{CO}_2} = 0.006$ bar), the only climatically significant source of water vapor to the atmosphere is the north polar cap. The north polar cap is cold because the atmosphere is too thin to provide much heat to it. Because the north polar cap is so cold, global average water vapor column abundance is $\sim 10 \mu\text{m}$. As a result, neither water vapor nor cloud ice is sufficiently abundant to greatly affect planet-averaged surface temperature. The cold polar temperature, enabled by the low p_{CO_2} of modern Mars, enforces hyper-aridity and prevents a warm climate on Mars today (27). A cloud greenhouse effect may be important at higher obliquity (e.g., ref. 28), associated with modestly elevated (still < 0.1 bar) p_{CO_2} .

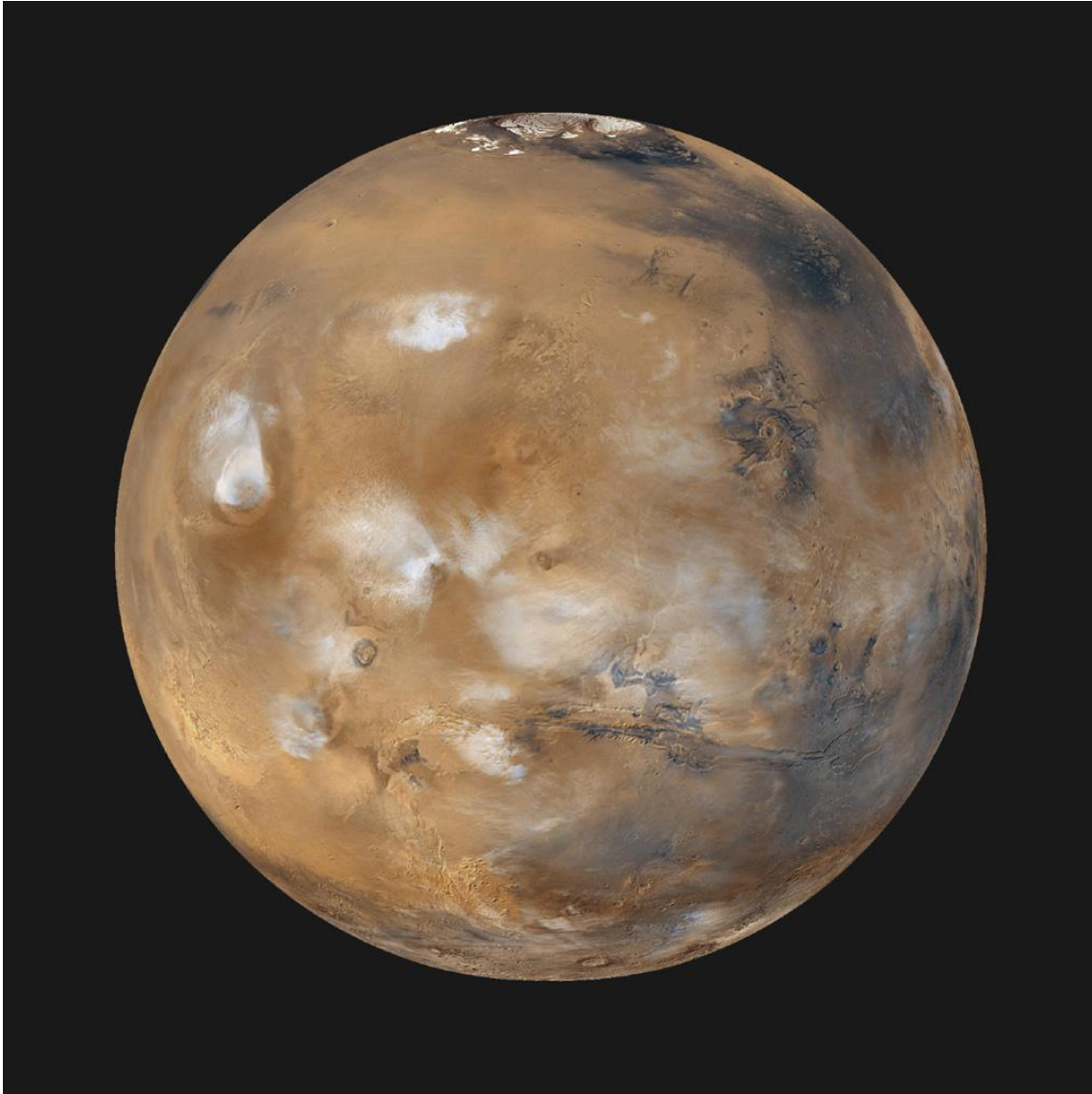


Fig. S1. Water ice clouds on modern Mars. April, 1999 mosaic of ~10 low-orbit Mars Global Surveyor (MGS) Mars Orbiter Camera Wide Angle (MOC-WA) visible-light images, projected onto a sphere with center of view at 15°N, 90°W. White features are water ice clouds (except for the water ice polar cap at the top of the image). The optically thickest clouds (left of image) are associated with Alba Mons and Olympus Mons. Diffuse water ice clouds cover much of the right of the image. Water ice clouds on Mars today are not extensive enough, optically thick enough, and (on average) at high enough altitude to provide strong surface warming. However, water ice clouds are believed to become important at high obliquity on <1 Gya Mars (e.g., 28), and have been proposed to be a key agent of warming on early Mars (e.g., 5). The latter hypothesis is the subject of the present paper. Image: NASA PIA02653 (NASA/JPL/Malin Space Science Systems).

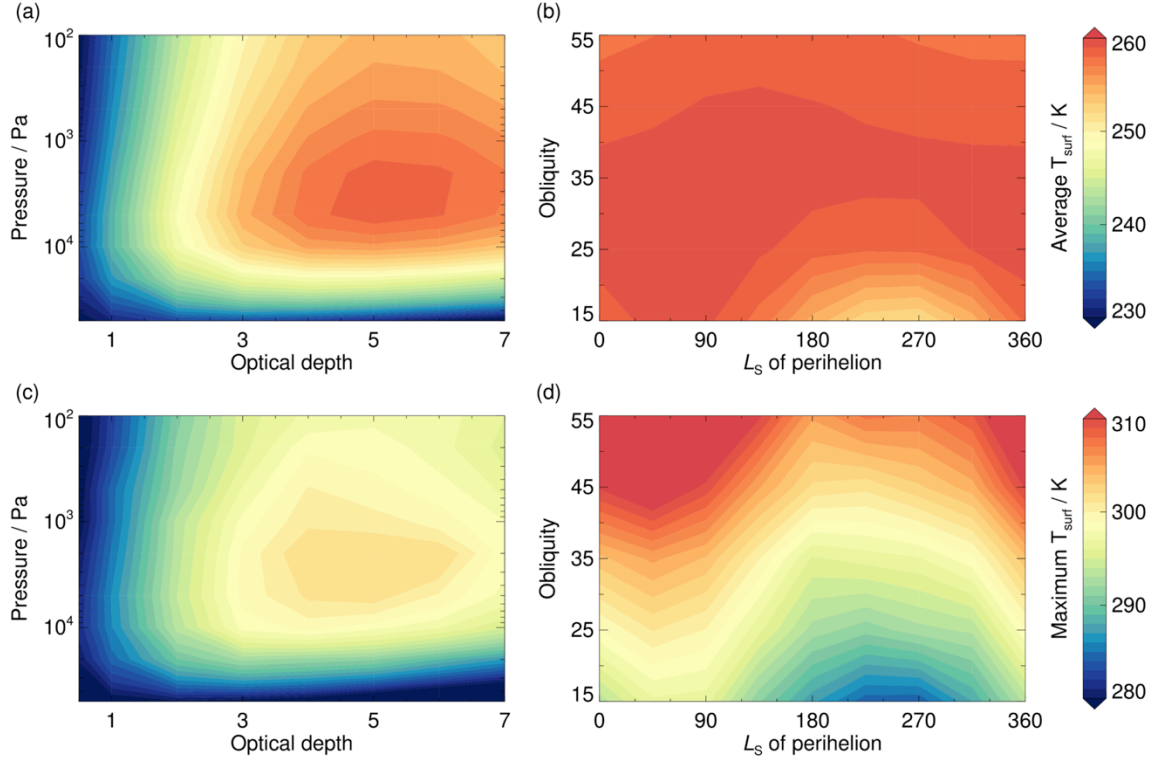


Fig. S2. Global climate model tests: Area-weighted average surface temperatures (top row), and maximum surface temperatures (bottom row), from GCM simulations with a prescribed cloud deck covering the globe at all times. Note change in color scales between the average and maximum temperatures. In **(a,c)** the global cloud optical depth and central pressure was varied for a circular orbit. In **(b,d)** the orbital parameters were varied for a cloud layer with an optical depth of 5 centered at 0.003 bar.

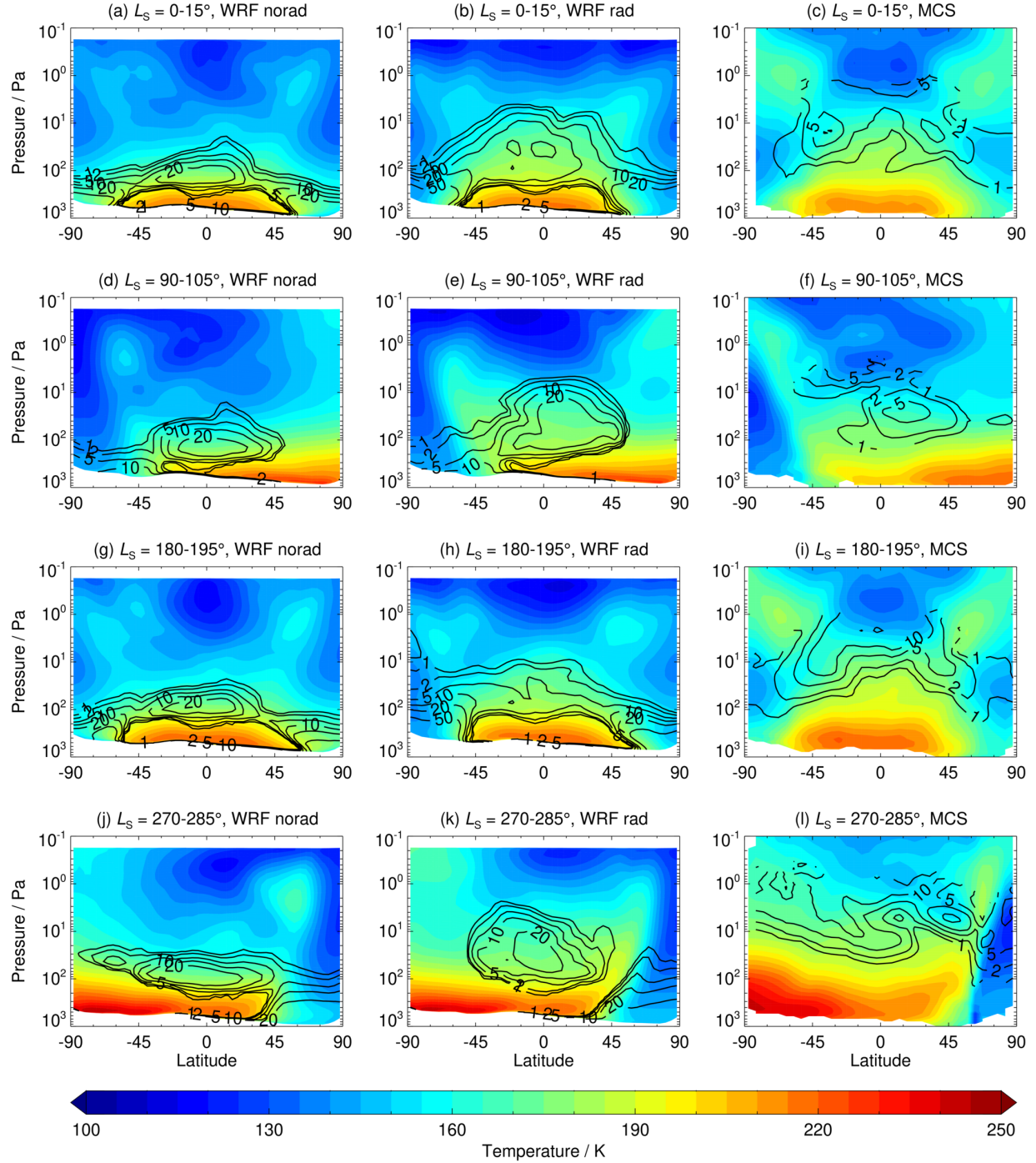


Fig. S3. Comparison between zonally-averaged nighttime temperatures (shaded) and water ice mass mixing ratios (black contours, units of ppm) at four different seasons. Shown are (left column) output from MarsWRF simulation with radiatively-inactive clouds, (center column) output from MarsWRF simulation with radiatively-active clouds, and (right column) data from Mars Climate Sounder (29). The simulations were performed with $p\text{CO}_2 = 0.006$ bar, as for present-day Mars, and data are averaged over 15° of solar longitude L_s , as labeled above each plot.

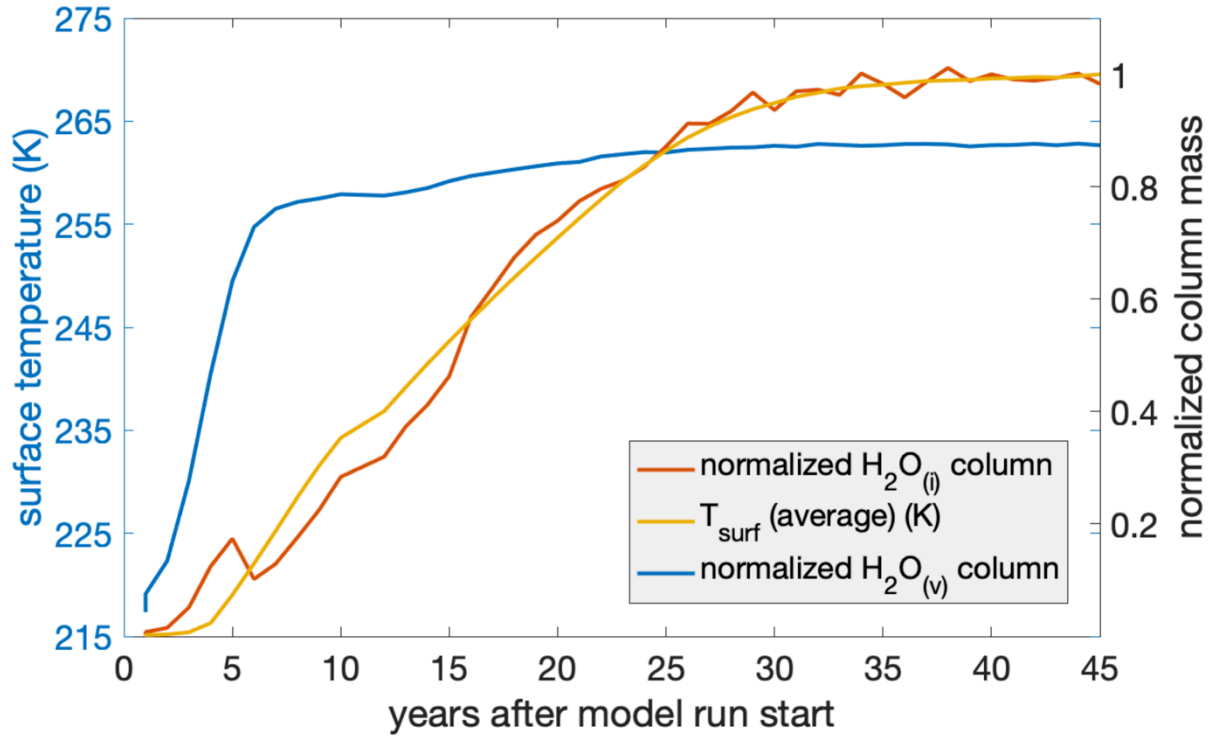
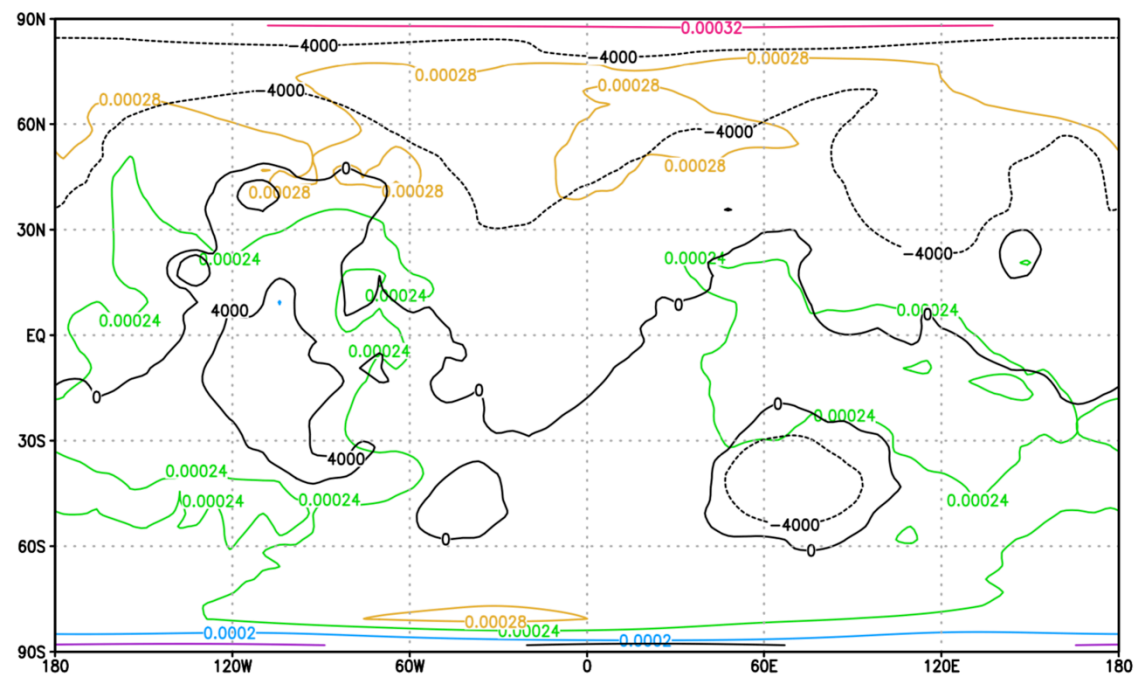
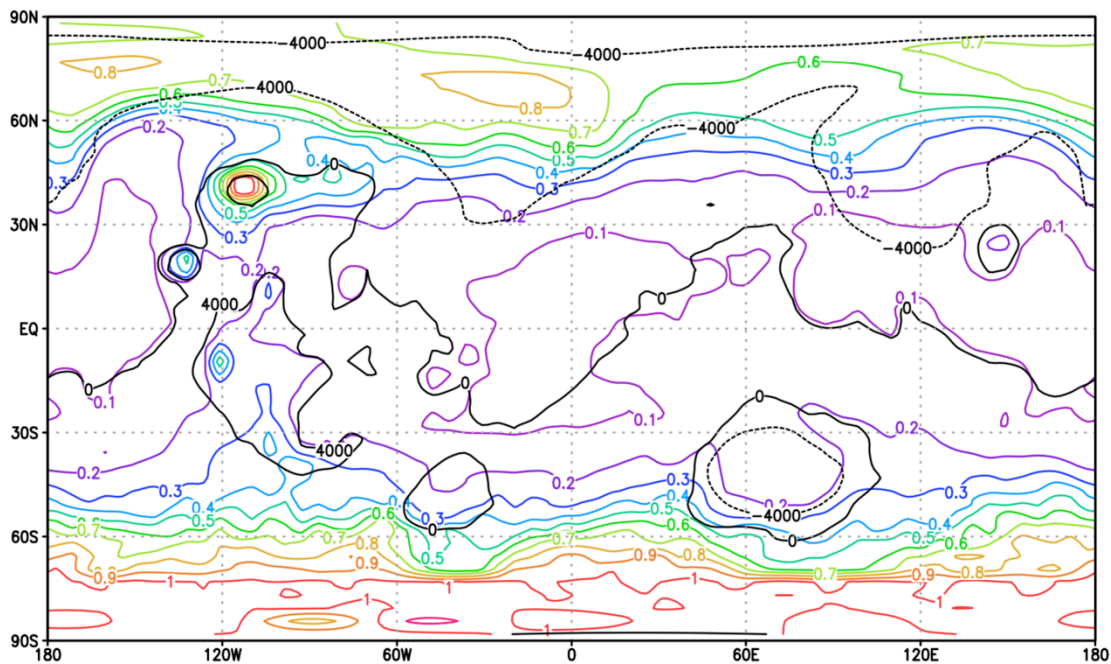


Fig. S4. Global climate model output: model spin-up for a cold/dry initial condition leading to the climate shown in Fig. 1, showing steady state mass balance for modeled surface H₂O reservoirs. Steady state mass balance is observed both globally, as shown here, and also locally. The column masses (pr- μm) are normalized to values of $33 \mu\text{m}$ for ice and $4 \times 10^3 \mu\text{m}$ for water vapor.

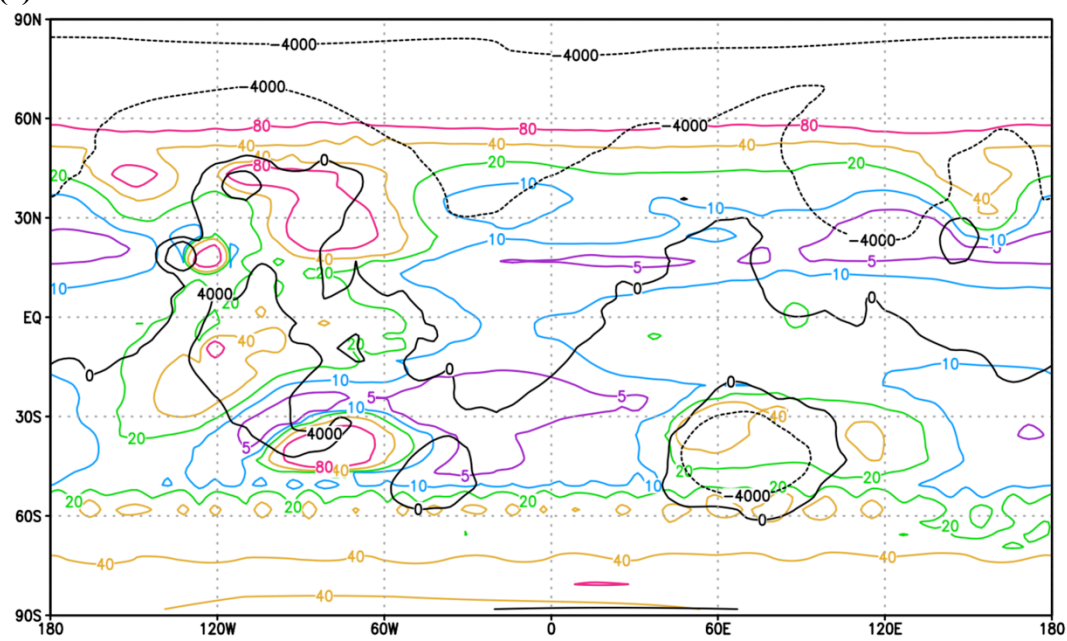
(a)



(b)



(c)



(d)

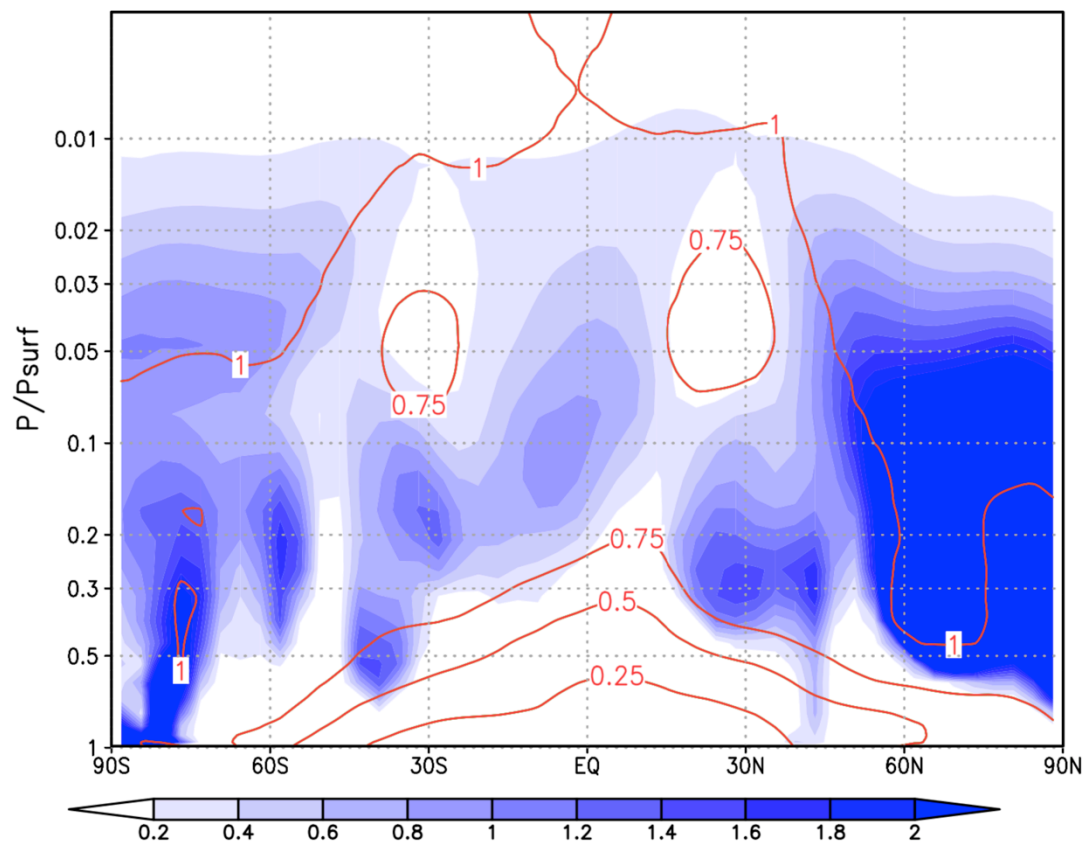
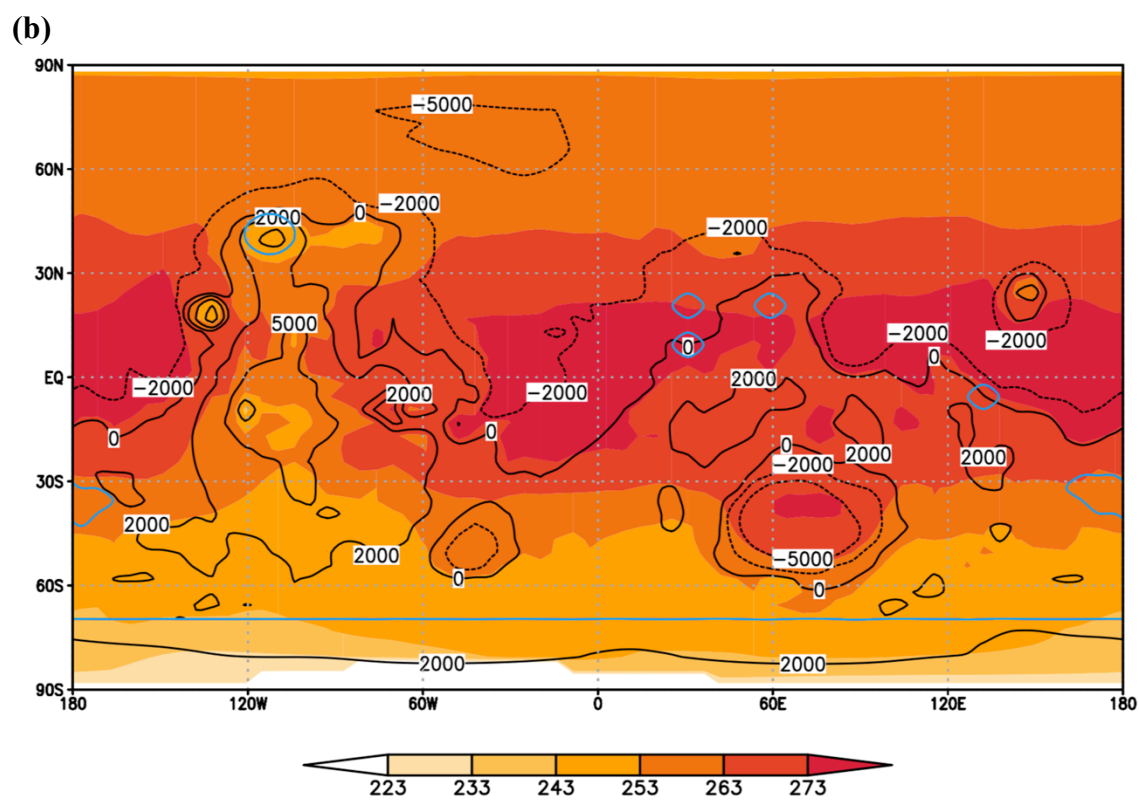
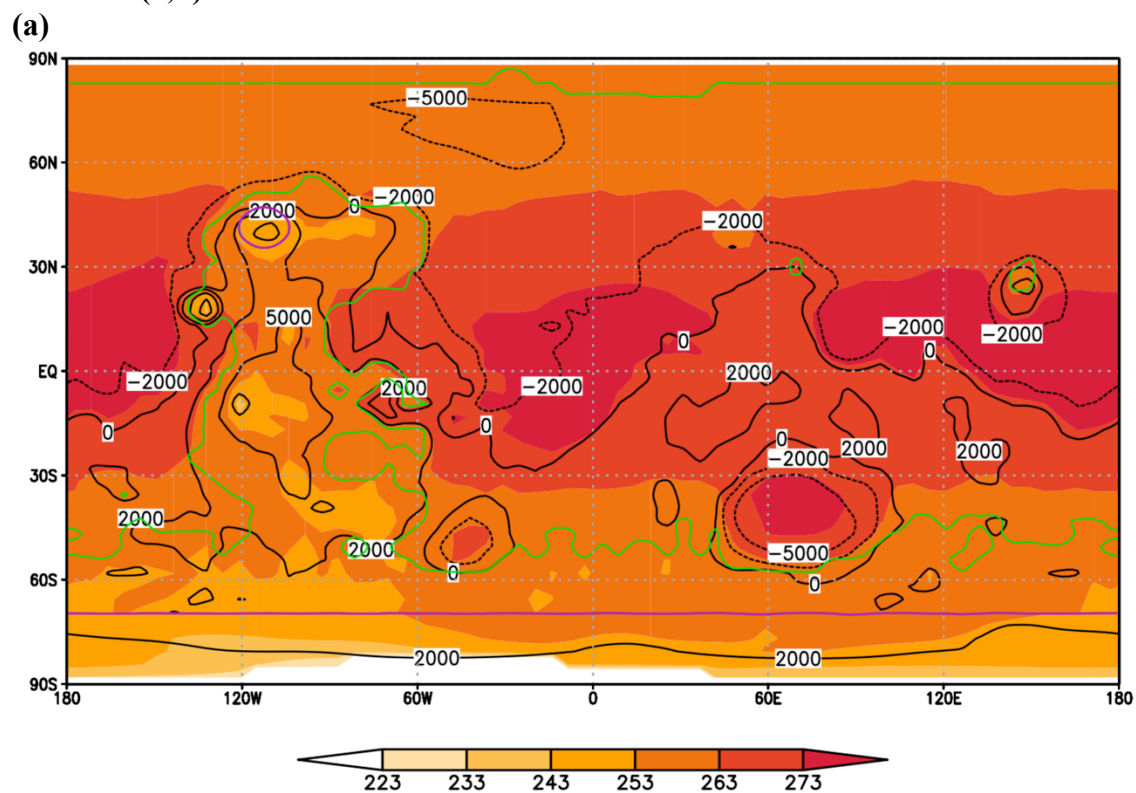


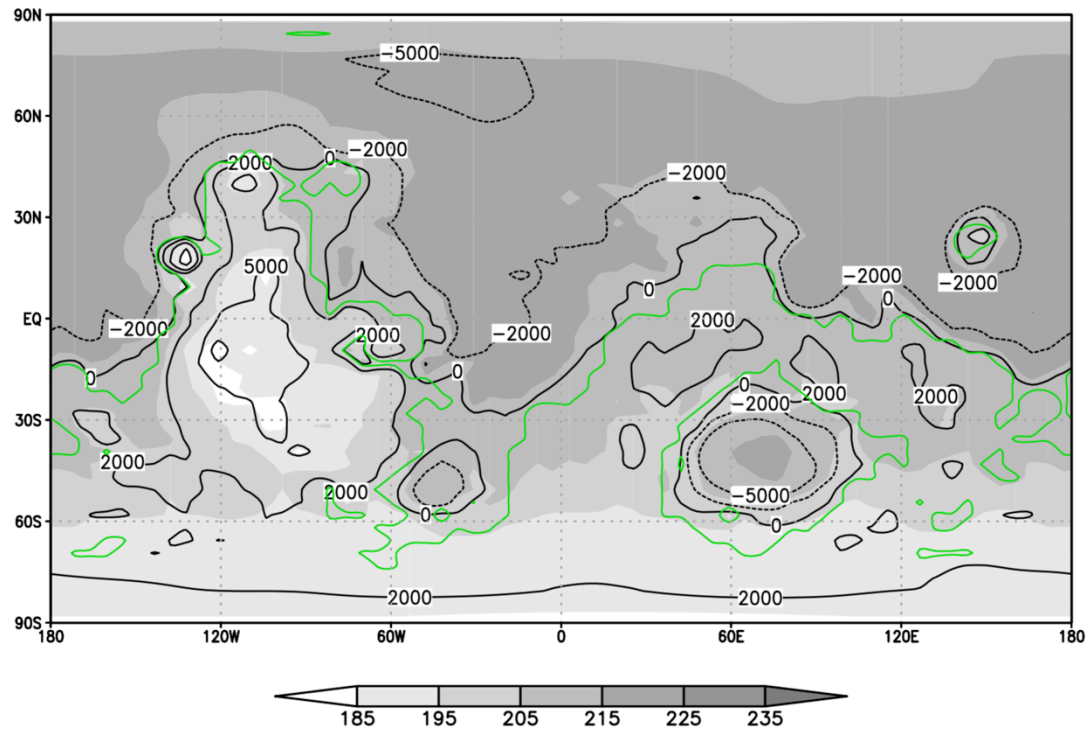
Fig. S5. Further details of a warm-climate equilibrium outcome corresponding to Fig. 1. In each panel, black contours show topography in meters. **(a)** Colored contours correspond to the atmospheric water vapor mixing ratio (kg/kg) low in the atmosphere ($P/P_{\text{surf}} \sim 0.9$). Water vapor is well-mixed (close to uniform); high elevations away from perennial surface H_2O deposits are slightly drier. **(b)** Colored contours correspond to relative humidity evaluated using the atmospheric temperatures and vapor mixing ratio for the lowest model atmospheric layer. Average near-surface humidity is $<30\%$ in our runs. **(c)** Colored contours correspond to the water ice cloud column in precipitable μm from Fig. 1. The water-ice column is thickest downwind of the major volcanoes and at high latitudes. **(d)** As Fig. 1a, but showing zonally-averaged, annual average cloud ice water content (mg/m^3 ; color shading) and zonally averaged, annual-average relative humidity (red contours). Nonzero average ice abundances in areas with average relative humidity < 1 are due to the time/zonal averaging.

(a,b): ARID CLIMATE ROBUSTLY MAINTAINS GLOBAL WARMTH



(c,d): EXTENSIVE SURFACE WATER ICE LEADS TO A HIGH RELATIVE HUMIDITY CLIMATE THAT FAILS TO PROVIDE STRONG CLOUD WARMING

(c)



(d)

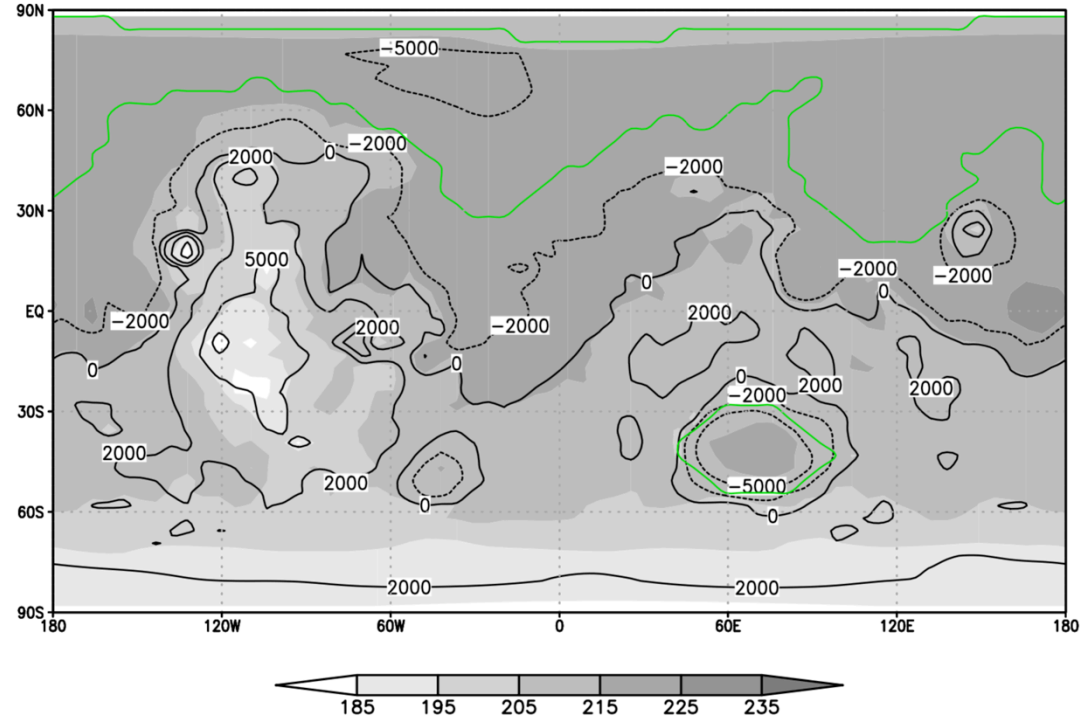


Fig. S6. Global climate model sensitivity tests. Color shading corresponds to annual-average surface temperatures, \bar{T} (K). Black contours correspond to Mars topography (m). (a,b) show that climates with a spatially restricted distribution of surface water ice robustly maintain global warmth. However, (c,d) show that more extensive surface water ice distributions produce cold climates. **(a)** As in Fig. 1b, but imposing an eccentricity of 0.1 and obliquity of 25° (similar to modern Mars), and showing the mean temperature for the ~ 100 sol equatorial warm season. Water ice locations (purple outline) are the same as in Fig. 1b. The green contour encloses the very large region that has a continuous 100-sol season with $\bar{T} > 273\text{K}$ during every Mars year. **(b)** As in Fig. 1b, but adding a sea in Eridania as well as large lakes at Gale, Antoniadi, Cassini, and Tikhonravov (total area $\sim 600,000 \text{ km}^2$) (18). Surface H_2O locations are shown in blue contours. **(c)** Climate resulting from an initial surface water ice deposit at all elevations above +1 km (above green contour). This leads to a cold climate with $\Delta T_{w-c} = 13 \text{ K}$ and $\bar{T} = 209 \text{ K}$. Ice migrates in this simulation to high ground, with the Tharsis region being especially favorable for H_2O ice accumulation (consistent with 30). **(d)** Climate forced by water ice at all elevations below -4 km (below green contour). This corresponds to an ice-covered Northern ocean and an ice-covered Hellas sea. A cold climate results ($\bar{T} = 212 \text{ K}$).

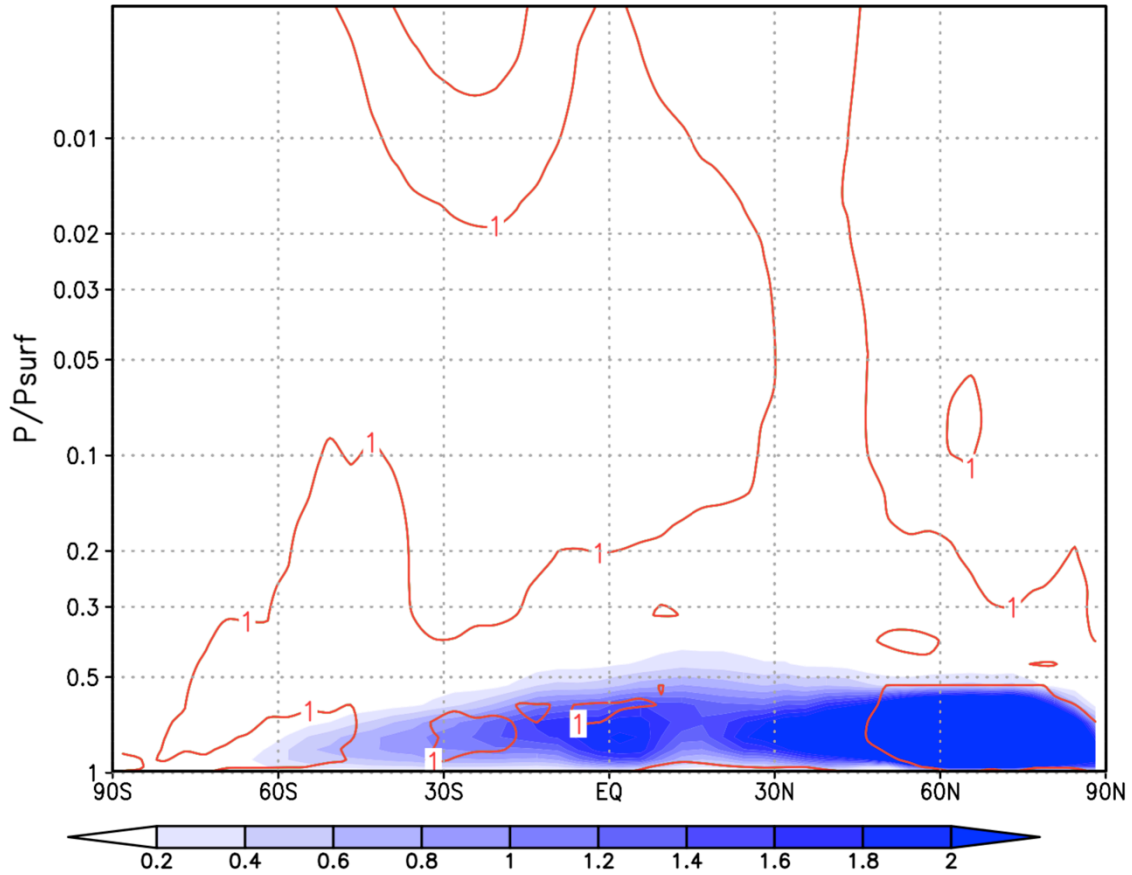


Fig. S7. Global climate model output: as in Fig. 1a, but showing results from a simulation for extensive surface water ice (water ice at all elevations above +1 km, Fig. S6c). This leads to a cold climate with $\Delta T_{w-c} = 13$ K and $\bar{T} = 209$ K and high average surface relative humidity (84%). Zonally averaged, annual-average cloud water ice mass mixing ratio (ppm by weight; color shading); and zonally averaged, annual-average relative humidity (red contours). Y-axis uses terrain-following σ coordinates ($\sigma = P/P_{\text{surf}}$). Nonzero average ice abundance in areas with average relative humidity < 1 are due to the time/zonal averaging.

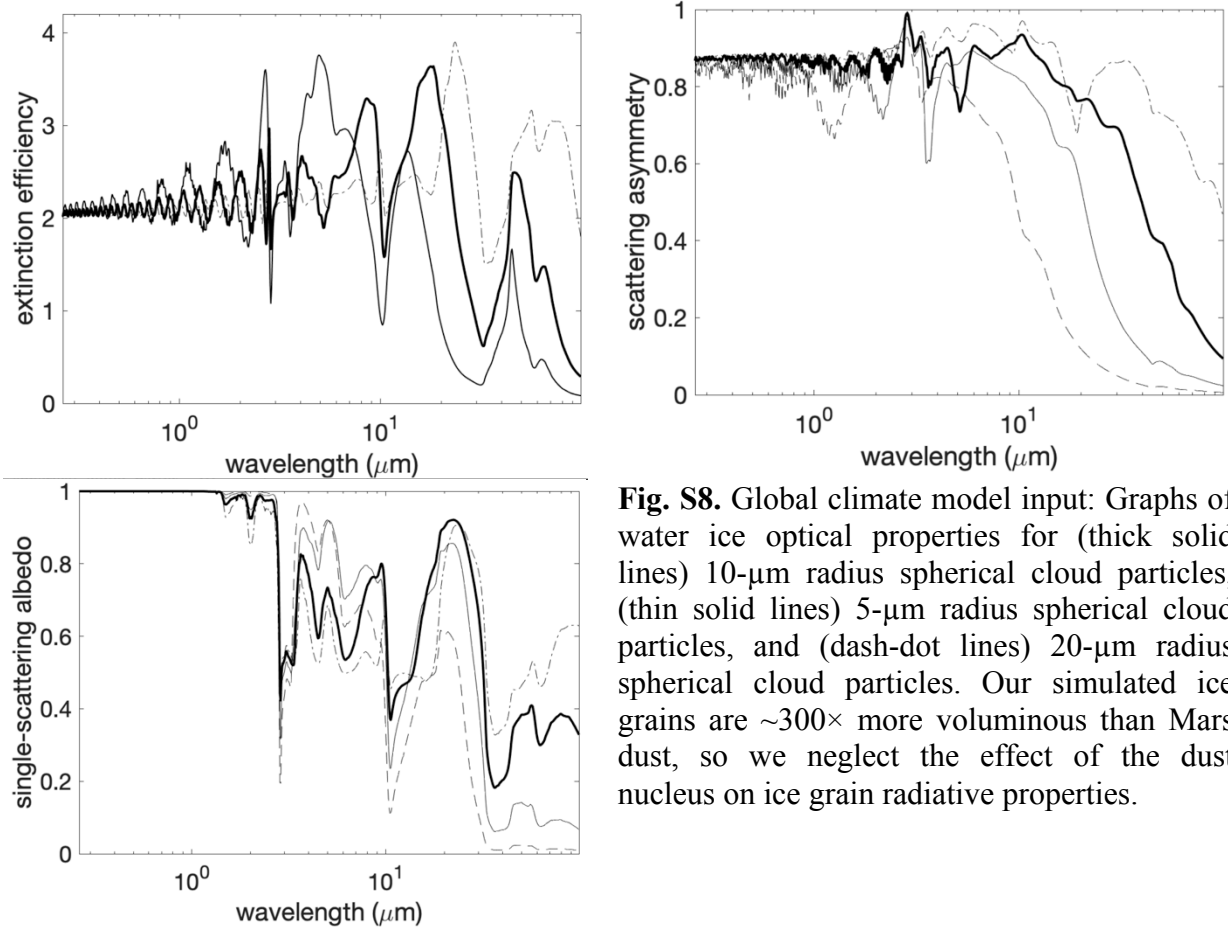


Fig. S8. Global climate model input: Graphs of water ice optical properties for (thick solid lines) 10- μm radius spherical cloud particles, (thin solid lines) 5- μm radius spherical cloud particles, and (dash-dot lines) 20- μm radius spherical cloud particles. Our simulated ice grains are $\sim 300\times$ more voluminous than Mars dust, so we neglect the effect of the dust nucleus on ice grain radiative properties.

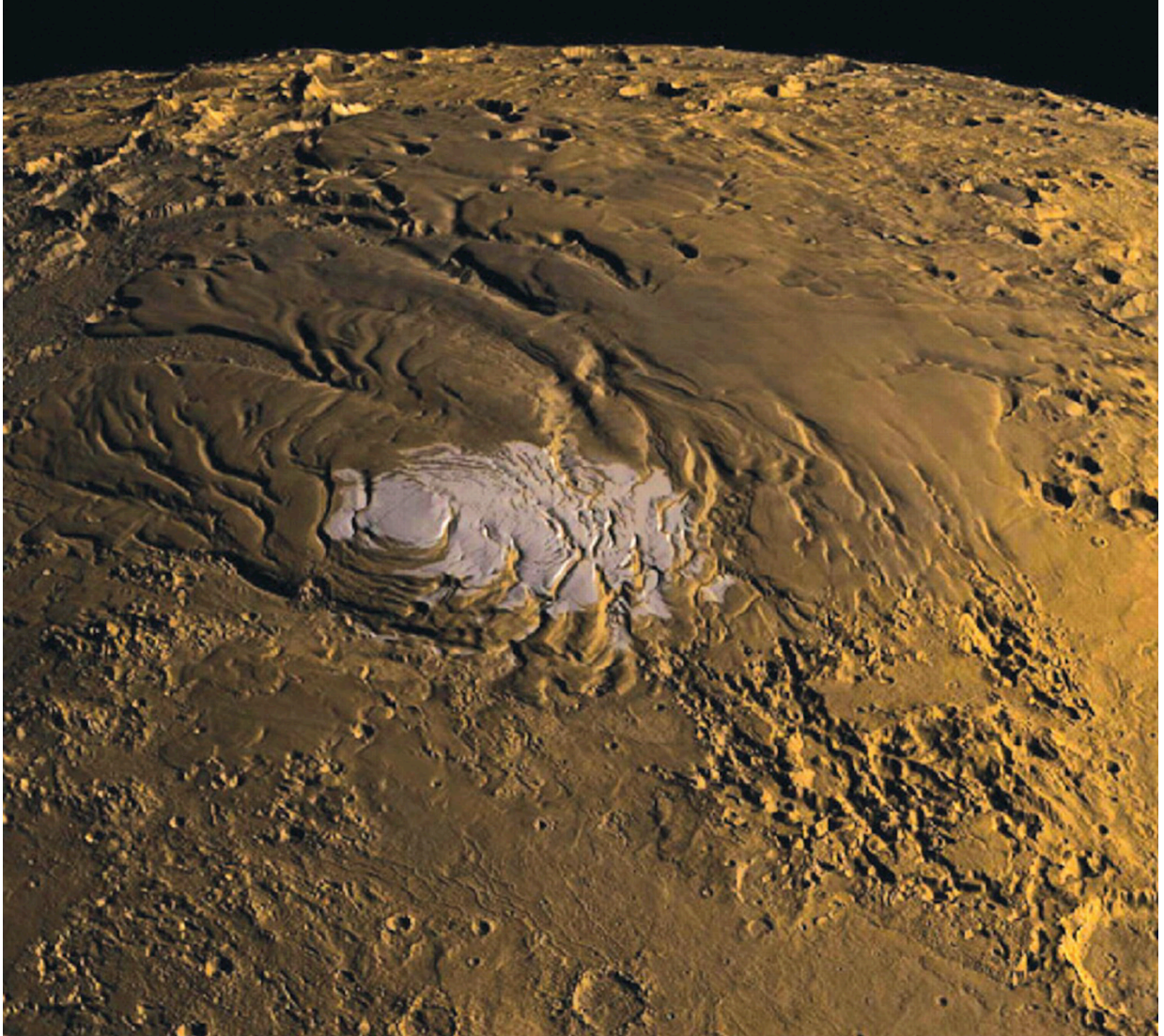


Fig. S9. Visualization (credit: NASA / MOLA Science Team) of the sublimation-lag-covered H₂O-ice-dominated deposit near the South Pole of Mars, from ref. 31. The smooth dome, lacking obvious craters, at the center of the visualization is primarily dust-mantled water ice (water ice volume $\sim 10^6$ km³; the smaller white area corresponds to perennial CO₂ ice). Very little H₂O-ice is exposed in the spacecraft era, even though radar data show that the dust mantle is topographically trivial (<10 m thick) and that the smooth dome is primarily H₂O-ice. As a result of dust-mantle isolation of the South Pole ice from the atmosphere, the spacecraft-era water cycle is driven by the H₂O ice cap near the North Pole of Mars. This demonstrates that the waxing and waning of stratigraphically trivial (<10 m thick in this case) sublimation lag deposits can greatly affect the aridity of Mars.

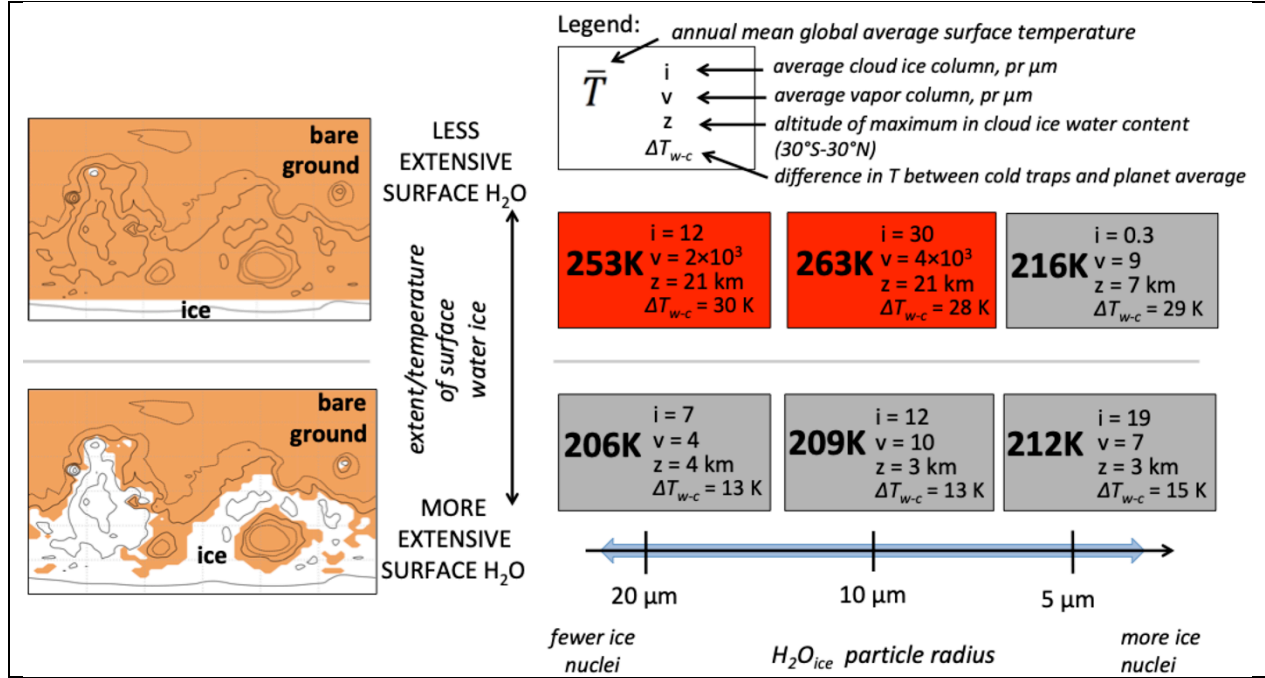


Fig. S10. This is a more detailed version of Fig. 2 from the main text. Control of Mars climate by extent of surface H_2O cover and by ice cloud particle size. Left column shows ice distribution for each row (black topography contours are the same as in Fig. 1). The other columns show (for each run) average temperatures (\bar{T} , in K), average vapor columns (“v”, pr- μm), average cloud ice columns (“i”, pr- μm), and the altitudes of low-latitude (30°S - 30°N) cloud ice water content maxima. For ΔT_{w-c} , here we define the spatial average cold trap temperature as the characteristic cold trap temperature. For example, the 10 μm run in the top row (Fig. 1) corresponds to a run with fixed cloud particle radius of 10 μm , and the water ice extent shown in the top map. Warm-climate equilibrated outcomes are shown in red, cold-climate equilibrated outcomes in gray. Results are for cold/dry-starts. Double-headed blue arrow corresponds to wide range of spacecraft-era Mars cloud $\text{H}_2\text{O}_{\text{ice}}$ radii (2-70 μm , ref. 32).

Supplementary references

1. Ramirez, R.M., and J. Kasting, 2017, Could cirrus clouds have warmed early Mars?, *Icarus*, 281, 248-261.
2. Turbet, M., C. Gillmann, F. Forget, B. Baudin, A. Palumbo, J. Head, and Ö. Karatekin, 2020, The environmental effects of very large bolide impacts on early Mars explored with a hierarchy of numerical models, *Icarus* 335, 113419.
3. Steele, L.J., S.R. Lewis, and M.R. Patel, 2014, The radiative impact of water ice clouds from a reanalysis of Mars Climate Sounder data, *Geophysical Research Letters*, 41(13), 4471-4478.
4. Turbet, M; Boulet, C; Karman, T, 2020a, Measurements and semi-empirical calculations of $\text{CO}_2 + \text{CH}_4$ and $\text{CO}_2 + \text{H}_2$ collision-induced absorption across a wide range of wavelengths and temperatures. Application for the prediction of early Mars surface temperature, *Icarus* 346, article id. 113762.
5. Urata, R.A., and O.B. Toon, 2013, Simulations of the martian hydrologic cycle with a general circulation model: Implications for the ancient martian climate, *Icarus*, 226, 229-250.
6. Richardson, M.I., A.D. Toigo, and C.E Newman, 2007, PlanetWRF: A general purpose, local to global numerical model for planetary atmospheric and climate dynamics, *J. Geophys. Res.*, 112, E9, E09001.
7. Lee, C., Richardson, M.I., Newman, C.E., and Mischna, M.A., 2018, The sensitivity of solstitial pauses to atmospheric ice and dust in the MarsWRF General Circulation Model, *Icarus*, 311, 23-34.
8. Natarajan, M., Dwyer Cianciolo, A., Fairlie, T.D., et al. 2015, Sensitivity of simulated Martian atmospheric temperature to prescribed dust opacity distribution: Comparison of model results with reconstructed data from Mars Exploration Rover missions, *Journal of Geophysical Research (Planets)*, 120, 2002.
9. Fonseca, R.M.; Zorzano, M.-P.; Martín-Torres, J., 2019, MARSWRF Prediction of Entry Descent Landing Profiles: Applications to Mars Exploration, *Earth and Space Science*, 6, 1440-1459
10. Guzewich, S.D.; Newman, C. E.; de la Torre Juárez, M.; Wilson, R. J.; Lemmon, M.; Smith, M. D.; Kahanpää, H.; Harri, A.-M., 2016a, Atmospheric tides in Gale Crater, Mars, *Icarus*, 268, 37-49.
11. Newman, C.E.; Gómez-Elvira, J.; Marin, M.; Navarro, S.; Torres, J.; Richardson, M.I.; Battalio, J.M.; Guzewich, S.D.; Sullivan, R.; de la Torre, M.; Vasavada, A.R.; Bridges, N.T., 2017, Winds measured by the Rover Environmental Monitoring Station (REMS) during the Mars Science Laboratory (MSL) rover's Bagnold Dunes Campaign and comparison with numerical modeling using MarsWRF, *Icarus*, 291, 203-231.

12. Fonseca, R. M.; Zorzano-Mier, M.-P.; Martín-Torres, J., 2018, Planetary boundary layer and circulation dynamics at Gale Crater, Mars, *Icarus*, 302, p. 537-559.
13. Wilson, R. John, 1997, A general circulation model simulation of the Martian polar warming, *Geophysical Research Letters*, 24, 123-126.
14. Guzewich, S.D., Toigo, A. D., Waugh, D. W., 2016b, The effect of dust on the martian polar vortices, *Icarus* 278, 100-118.
15. Smith, M.D., 2004, Interannual variability in TES atmospheric observations of Mars during 1999-2003, *Icarus*, 167, 148-165.
16. Heavens, N.G., J.L. Benson, D.M. Kass, A. Kleinböhl, W.A. Abdou, D.J. McCleese, M.I. Richardson, J.T. Schofield, J.H. Shirley, and P.M. Wolkenberg, 2010, Water ice clouds over the Martian tropics during northern summer, *Geophys. Res. Lett.*, 37, L18202.
17. Kleinböhl, A.; Schofield, J.T.; Kass, D.M.; Abdou, W.A.; Backus, C.R.; Sen, B.; Shirley, J.H.; Lawson, W.G.; Richardson, M.I.; Taylor, F.W.; Teanby, N.A.; McCleese, D.J., 2009, Mars Climate Sounder limb profile retrieval of atmospheric temperature, pressure, and dust and water ice opacity, *Journal of Geophysical Research*, 114, CiteID E10006.
18. Fassett, C.I., and J.W. Head, 2008, Valley network-fed, open-basin lakes on Mars: Distribution and implications for Noachian surface and subsurface hydrology, *Icarus* 198, 37–56.
19. Pierrehumbert, R., 2010, *Principles of planetary climate*, Cambridge University Press.
20. Popp, M.; Schmidt, H.; Marotzke, J., 2015, Initiation of a Runaway Greenhouse in a Cloudy Column, *J. Atmos. Sci.*, 72, 452-471.
21. Wordsworth, R., F. Forget, E. Millour, J.W. Head, J.-B. Madeleine, B. Charnay, 2013, Global modelling of the early Martian climate under a denser CO₂ atmosphere: water cycle and ice evolution. *Icarus* 222, 1–19.
22. Levy, J.S., et al., 2014, Sequestered glacial ice contribution to the global Martian water budget: Geometric constraints on the volume of remnant, midlatitude debris-covered glaciers, *Geophys. Res. Lett.*, 119(10), 2188-2196.
23. Schorghofer, N., 2007, Theory of ground ice stability in sublimation environments, *Phys. Rev. E* 75, 041201.
24. Montmessin, F., R.M. Haberle, F. Forget, Y. Langevin, R.T. Clancy, and J.-P. Bibring, 2007, On the origin of perennial water ice at the south pole of Mars: A precession-controlled mechanism?, *J. Geophys. Res.*, 112(E8), E08S17.

25. Emmett, J.A., J. R. Murphy, Melinda A. Kahre, 2020, Obliquity dependence of the formation of the martian polar layered deposits, *Planetary and Space Science* 193, 105047.
26. Mischna, M.A., and M.I. Richardson, 2005, A reanalysis of water abundances in the Martian atmosphere at high obliquity, *Geophys. Res. Lett.*, 32(3).
27. Jakosky, Bruce M.; Edwards, Christopher S., 2018, Inventory of CO₂ available for terraforming Mars, *Nature Astronomy*, 2, 634-639.
28. Madeleine, J.-B., J.W. Head, F. Forget, T. Navarro, E. Millour, A. Spiga, A. Colaitis, A. Määttänen, F. Montmessin, and J.L. Dickson, 2014, Recent ice ages on Mars: The role of radiatively active clouds and cloud microphysics, *Geophys. Res. Lett.*, 41, 4873-4879.
29. McCleese, D. J., N.G. Heavens, J.T. Schofield, W.A. Abdou, J.L. Bandfield, S.B. Calcutt, P.G. Irwin, D.M. Kass, A. Kleinböhl, S.R. Lewis, D.A. Paige, P.L. Read, M.I. Richardson, J.H. Shirley, F.W. Taylor, N. Teanby, and R.W. Zurek, 2010, Structure and dynamics of the Martian lower and middle atmosphere as observed by the Mars Climate Sounder: Seasonal variations in zonal mean temperature, dust, and water ice aerosols, *J. Geophys. Res.*, 115, E12016.
30. Wordsworth, R.D., L. Kerber, R.T. Pierrehumbert, F. Forget, and J.W. Head, 2015, Comparison of "warm and wet" and "cold and icy" scenarios for early Mars in a 3-D climate model, *J. Geophys. Res.*, 120, 1201-1219.
31. Zuber, M.T., R.J. Phillips, J.C. Andrews-Hanna, S.W. Asmar, A.S. Konopliv, F.G. Lemoine, J.J. Plaut, D.E. Smith, and S.E. Smrekar, 2007, Density of Mars' south polar layered deposits, *Science*, 317(5845), 1718-1719.
32. Clancy, R.T., F. Montmessin, J. Benson, F. Daerden, A. Colaprete, and M.J. Wolff, 2017, Mars Clouds, in *The atmosphere and climate of Mars*, Edited by R.M. Haberle et al. Cambridge University Press, p. 42-75.